NTNU – Trondheim
Norwegian University of
Science and Technology

Precipitate Structure Changes during Overaging in an Al-Mg-Si Alloy

Jason Daniel David A. Granholt

Master of Science in Physics and Mathematics
Submission date: June 2012
Supervisor: Randi Holmestad, IFY

Norwegian University of Science and Technology
Department of Physics

Precipitate Structure Changes during Overaging in an Al-Mg-Si Alloy

Jason Daniel David Andersen Granholt

June 15, 2012

Abstract

Starting from a super saturated solid solution and two different conditions with β'' precipitates (T6) an Al-Mg-Si alloy was heat treated at 200°C and investigated by hardness measurements. One of the T6 conditions was investigated with transmission electron microscopy (TEM). The phase transformation to post-β'' was studied with TEM and there was found that post-β'' phases nucleated on the β'' particles. After longer overaging times the growths were larger. A simple model was proposed , and it suggested that the growth of post- β'' phases was the first steps in the transformation of β'', and that the final result was a microstructure consisting only of post- β'' particles.

Sammendrag

Med utgangspunkt i en mettet faststoff løsning og to forskjellige betingelser med β'' presipitater (T6) ble en Al-Mg-Si legering varmebehandlet på 200°C og undersøkt med hardhetsmålinger. En av T6 betingelsene ble undersøkt med transmisjons elektron mikroskopi (TEM). Faseovergangen til post- β'' ble studert med TEM og det ble funnet at post- β'' faser kimdannet på β'' partiklene. Etter lang tid med overaldring hadde vekstene som ble dannet under kimdanningen blitt større. En enkel modell ble foreslått, og den antydet at veksten av post- β'' faser var det tidlige stadiet i transformasjonen av β'', og at det endelige resultatet var en mikrostruktur bestående av kun post- β'' partikler.

Preface

This master thesis was written during the spring of 2012 as a part of my master's degree in technological physics at the Norwegian University of Science an Technology, NTNU. The work was carried out at the division of condensed matter physics.

This thesis is a continuation of my project thesis written during the autumn of 2011. Some of the results and other content in that thesis are therefore included here.

I would like to thank my supervisors, Professor Randi Holmestad and research scientist Calin D. Marioara from SINTEF Materials and chemistry for their guidance. I would also like to thank Bjørn Solheim for TEM training and PhD- student Sigurd Wenner for training and general advice.

Trondheim, June, 2012

Jason Granholt

List of Abbreviations

TEM - Transmission Electron Microscopy
SHT - Solution Heat Treatment
SSSS - Super Saturated Solid Solution
OA - Overaging
HT - Heat Treatment
HRTEM - High Resolution Transmission Electron Microscopy
HT1 - Heat Treatment One
HT2 - Heat Treatment Two
HT3 - Heat Treatment Three
FEG - Field Emission Gun
EELS - Electron Energy Loss Spectroscopy
ZLP - Zero Loss Peak
FFT - Fast Fourier Transform

Contents

Chapter 1

Introduction

There are many reasons for studying metals. An important reason is to optimize their applications in e.g buildings, cars, planes and packagings. The introduction of light weight metals into energy demanding applications is especially important, so that the use of fossil fuels can be reduced in order to get less pollution. One of these light weight metals is aluminium.

Aluminium is a common [1] metal found in large abundances in aluminium oxide. In order to get pure aluminium electrolysis is performed. Pure aluminium is very soft and does not have many applications. But there are two factors that will give a major change in the strength. The first is by adding alloying elements to the pure aluminium. This will result in a mixture of aluminium and other elements, called an alloy. The second factor is to heat up and cool down the alloy in a certain way [2]. This is called heat treatment. This motivates some questions. What should the alloying elements be? What happens during heat treatment? The second question is of interest in this work. It is found that Al-Mg-Si alloys have good properties and is therefore chosen for further study. There are some problems regarding heat treatments. One of them will be described in the following way: Assume that the optimal sequence of heating and cooling the alloy is performed. Then the alloy will have optimal properties. But if the alloy for some reason would be placed at high temperatures again , this could be regarded as another step in the heating sequence, and thus the sequence is no longer optimal. These kinds of problems would only occur if there were such additional heat treatments. Practical examples of this would be any hot place after production were aluminium could be used, e.g close to the engine in a car. If a better understanding of what happens during heat treatment is obtained, the negative effects could possibly be reduced or even eliminated.

The reason for the increase in strength during heat treatment is that small particles rich in Mg and Si are formed. These are called precipitates and will hinder movement in the material, thus making the material harder to deform. This means a higher strength. In Al-Mg-Si alloys the precipitate formed after the optimal heat treatment (i.e the precipitate that gives the main hardening effect) is called β'' [3].

The purpose of this master thesis is to investigate how β'' changes when it is exposed to additional heat treatment. Two models for changing the particles will be proposed here, which are both conceptually simple. The first is that the β''

dissolves and then starts to grow another place in the aluminium matrix. This is known as dissolution, nucleation and growth. The other could be that the particle simply transforms into something else without moving. This is called on site transformation. The investigations will be done on one alloy type with different heat treatments. Hardness measurements will be obtained for each heat treatment and some samples will be chosen for further investigation in a transmission electron microscope (TEM). The TEM work will consist of collecting statistics for the particles and characterization of them by using a very high resolution. Then, the results will be compared to the previous suggestions and hopefully give a better understanding of how the transformation occurs.

Chapter 2

Theory

2.1 Aluminium

Aluminium is the most common metallic material on Earth´s crust, and the third most common material on the crust [1]. Aluminium is found in nature as aluminium oxide Al_2O_3 in minerals where the most common is a reddish stone called Bauxite. Electrolysis is the principal method for extracting aluminium. In its pure form aluminium is very soft, but when adding alloying elements the strength will increase dramatically. Adding a small amount of alloying elements will only change the density slightly. The reasons for the increase in strength is explained later. The increased strength with a negligible change in density results in a high strength/weight ratio compared to steel, since steel has a density about 3 times higher than the density of aluminium which is 2700 kg/m^3. Another important point is that recycling of aluminium only requires 5% of the extraction energy [4], making it very suitable for re-use.

2.1.1 Different alloy types

When referring to an aluminium alloy any mixture of aluminium with other elements can be considered. To organize all the possible mixtures, the alloys have been divided into different classes. The alloys are divided into two major branches which are called wrought alloys and casting alloys. These are again subdivided into heat-treatable and non-heat-treatable. Whether the alloys is wrought or casted depend on fabrication. Heat-treating properties depend on microstructure change when the material is kept at temperatures usually well above room temperature, and will be discussed later.

Table 2.1: An overview over the most common aluminium alloys.

Wrought alloys		Age hardenable
1xxx	Pure Al(>99.00 percent Al)	No
2xxx	Al-Cu and Al-Cu-Li	Yes
3xxx	Al-Mn	No
4xxx	Al-Si and Al-Mg-Si	Yes
5xxx	Al-Mg	No
6xxx	Al-Mg-Si	Yes
7xxx	Al-Mg-Zn	Yes
8xxx	others	-
Casting alloys		
1xx.x	Pure Al(>99.00 percent Al)	No
2xx.x	Al-Cu	Yes
3xx.x	Al-Si-Cu or Al-Mg-Si	No
4xx.x	Al-Si	No
5xx.x	Al-Mg	No
7xx.x	Al-Mg-Zn	Yes
8xx.x	Al-Sn	Yes
9xx.x	others	-

The alloys are classified by a labeling system with the label yxxx for wrought alloys and yxx.x for casting alloys. For wrought alloys y represent the main group of alloying elements and xxx represents the amount of alloying elements. The notation is similar for casting alloys, with the distinction that the last number stands for the product form. A list of the different types are given in table 2.1.

2.2   Microstructure

A perfect crystal model for a pure solid material is not sufficient to accurately describe the properties of a metal. Depending on what problem which is going to be solved, additional assumptions of the microstructure has to be made. For most cases in a real material, there will not be a continuous lattice throughout the bulk material. The material will be subdivided into small regions with different orientations which are called the **grains** of the material.

When other elements are added to pure Al, further possibilities for the system configuration will arise. It is found that when other elements are mixed with Al, they can group together and form particles referred to as precipitates.

2.2.1   Dislocations

Deviations from a perfect crystal can come in many forms. A common type of defect is a vacancy, which is simply a missing atom in the lattice. These are very important during heat-treatment and will be considered later.

A dislocation is a bigger fault involving whole(or partial) lattice planes, and has an impact on many atoms. There are two main types of dislocations.

The first is an edge dislocation, and is obtained by placing an extra half plane(or removing) between to other planes. In figure 2.1 a) the half plane is inserted between the third and the fourth vertical plane. This will force the nearest planes to adapt by bending so that the other planes remain along a continuous line. The bending is largest on the planes nearest to the new half plane. This bending results in different distances between the atoms, which again leads to lattice strains. If you make a closed loop by traversing around the dislocation with step size equal to the undistorted atomic distance, you will find that the number of steps below and above dislocation is different. This is seen in figure 2.1 a), when traversing the points MNOPQ. The vector between the starting and finishing points, M and Q, defines the burgers vector. A edge dislocation can be defined by this Burgers vector as it lies in the same plane as the path of propagation around the dislocation (MNOPQ) [5].

The other type is a dislocation that is obtained by gliding the lattice one atomic position, as seen in figure 2.1 b). The path of propagation is now perpendicular to the burgers vector, and this defines the screw dislocation [5]. This is seen in figure 2.1 b) where the undistorted plane MNOP is perpendicular to the burgers vector.

A process involving moving dislocations is called **slip**. The direction of motion is called the slip direction. Such motion will occur when the material is exposed to an external force. Slip occurs along the closest packed planes, because it requires the least energy.
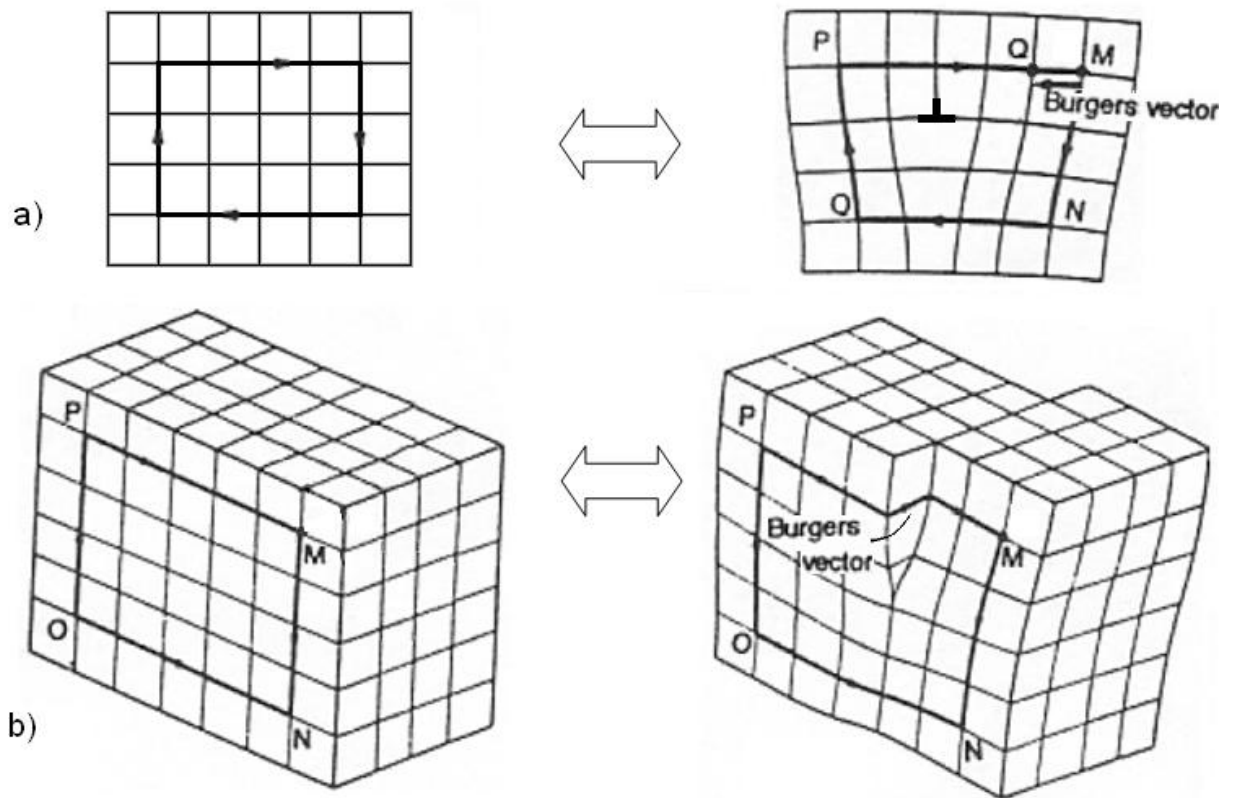
Figure 2.1: Burgers vector for a edge dislocation [6].

2.2.2   Coherency and strength

The degree of coherency tells us how much the structure in the precipitate differs from the crystal lattice. The coherency of a precipitate can be divided into 4 cases.
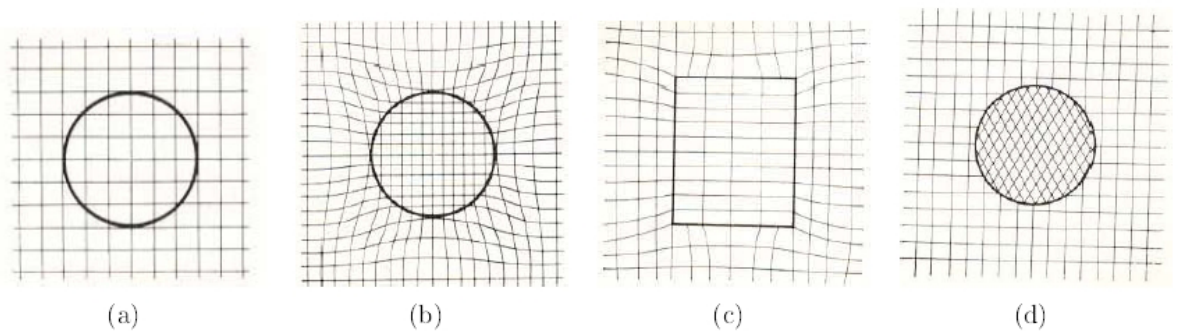

Figure 2.2: a) Fully coherent particle [7]. b) Coherent particle [7]. c) Partly coherent particle [7]. d) Incoherent particle [7].

Fully coherent particle: This case requires a perfect match between the precipitate and the matrix in all directions. This means that no planes are broken or bent. Visualized in figure 2.4a). No lattice strain is observed.

Coherent particle: There are still a continuous crossing of the boundary between the precipitate and the matrix. But there is a small misfit due to different

atom spacing seen in figure 2.4b). The bending of the lattice planes causes a strain field around the precipitate. Such a strain field will obstruct the movement of dislocations in for example a slip process. This makes the material more resistant to external forces, e.g it becomes harder.

Partially coherent particle: In this case there is a perfect match with one direction of the lattice, while there is a misfit between lattice and particle in another direction, see figure 2.4c). In this case it will also be a considerable strain field and thus a hardening effect.

Incoherent particle: Here both the orientation and crystal structure are different for the particle, see figure 2.4c). Here the strain field is lost and the hardening effect is small.

So the bulk material can become harder due to different degrees of coherency. This is not the only way to get a similar effect. The key property to a stronger metal was the decrease of movement in the microstructure. In the next section some other mechanisms are outlined.

2.2.3 Hardening mechanisms

Here some mechanisms for hardening a metal are quickly mentioned.

The precipitates mentioned in the previous section do not only hinder the dislocation movement indirectly through a strain field. The particles themselves hinder a movement of dislocations. This is called **particle hardening**.

As mentioned above, the material will consist of grains throughout the material. These grains will affect the strength. A small grain size will lead to a large amount of grain boundaries, which will then hinder the movement of dislocations. This will give a hardening effect.

In a solid solution the solute is different from the solvent. When a single atom of another type substitute the host lattice strain arises. As mentioned above, strain gives an hardening effect. The solute also often find stabilized positions on dislocations and thus preventing movement.

A material can also be hardened by deformation , which introduces dislocations. These dislocations will prevent movement of others. This called **work hardening**.

2.3 Hardness measurements

A common way to define hardness is a materials resistance to a non-reversible shape change when a force is applied. For example if a sharp object is pushed into a block of soft material it will be deformed by the object. If the same force is applied by pushing the object into hard metal the deformation will be much smaller , maybe just a small scratch in the surface. After the material is deformed the size of the deformation can be measured, and a measure of hardness will be obtained. The object deforming the material can vary. The Brinell hardness test uses a hard

sphere to make an indentation. In this work another shape will be used, and the method is called the Vickers hardness test.

2.3.1   The Vickers hardness test

When using the Vickers hardness test, there will be made an indentation in the material. Then the hardness is calculated from the size of the indentation. Specifically there is used a pyramid-shaped diamond indenter with a quadratic base. There is an angle of 136° between the two lateral faces. The load can be varied, but on automated intenders the load is usually fixed to 1 kg, 5 kg etc. In figure 2.3 below the diagonals from the indentation are in between red lines. The hardness value is obtained by measuring the length of these. The formula used for the hardness is given by

$$HV = \frac{2F sin(\frac{136°}{2})}{d^2} \tag{2.1}$$

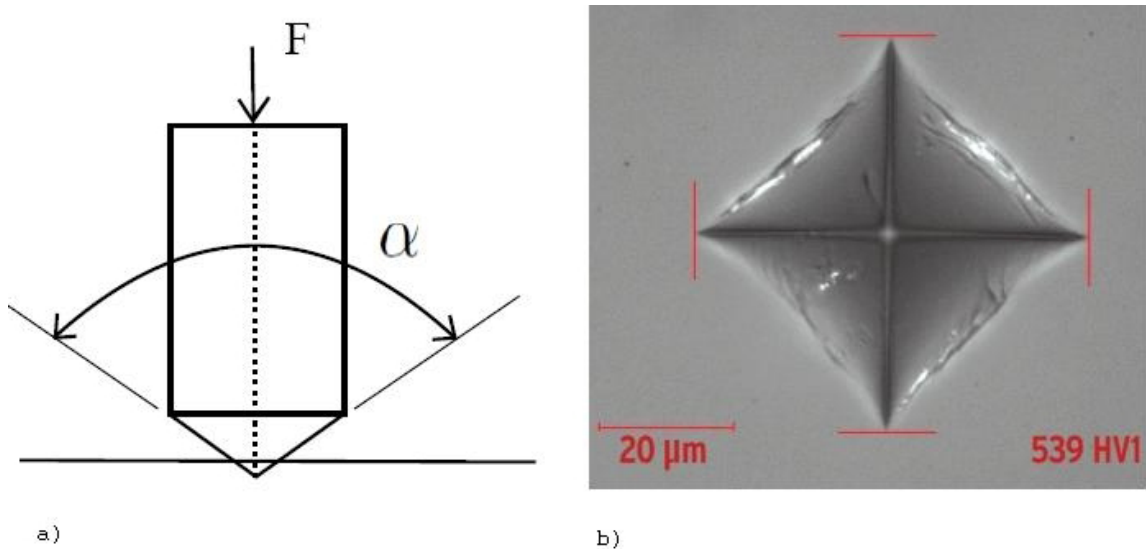where F is the load in kg and d is the mean value of the diagonals.

Figure 2.3: a) Schematic drawing of the indentor penetrating the surface [8]. b) A real indentation in a ceramic [9].

2.4   Thermodynamics

Basic knowledge of thermodynamics is required to understand the change taking place during microstructure evolution. Since the alloy studied will be in different phases, it is important to understand a phase diagram.

2.4.1   Phase Diagrams

Phase diagrams will be illustrated by a simple example. A binary phase diagram will be considered, where there are two elements A and B mixed together.

In Figure 2.4 a)-e) the free energy curves for the phases are given. The AB axis gives the fraction of each element. In this case the two phases are liquid and solid, but the phases could be of any type, e.g α phase of pure aluminium and $\alpha' + \beta$, aluminium in equilibrium with stable precipitates. In general there could also be more phases even tough the number of elements are the same. The phase at a certain fraction of solute at given temperature is found by the minimum in free energy. Then the phase diagram is obtained by transferring each of the (fraction)(phase) points for each temperature into a common diagram. For example in Figure 2.4 a) all the minimums will be given by the L curve, and thus all composition points along the horizontal line T1 in 2.4 f) gives a liquid phase. With free energies like the ones in 2.4 c), it can be shown that when it is possible to draw a common tangent that gives a lower energy, this then gives the minimum. The common tangent has a lower energy than either one of the free energy curves. We then have a mixed L and S phase, which is the area between solidus and liquidus lines given in 2.4 c).

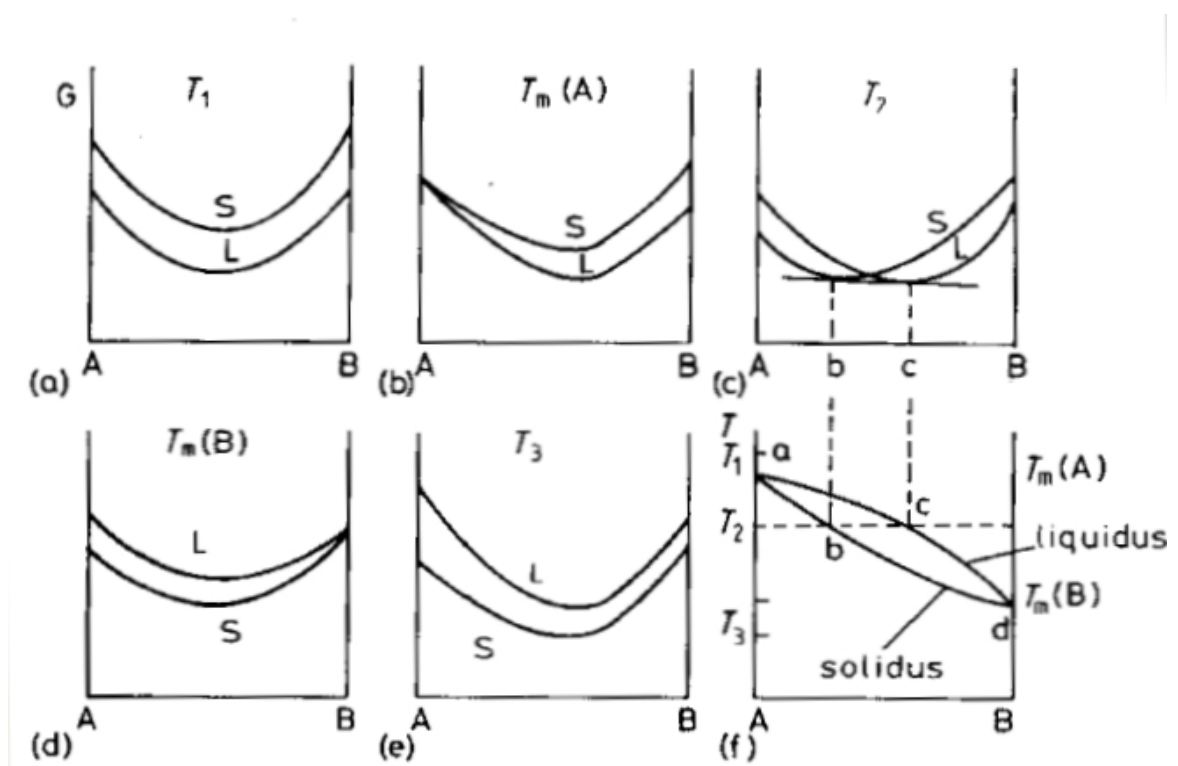The procedures is applicable to any phase diagram. But if the number of elements increase they become very complex.

Figure 2.4: The derivation of a simple phase diagram from the free energy curves for the liquid(L) and solid (S) [10].

2.5   Heat treatment of alloys

In order to get the desired hardening effect mentioned in section 2.2.2, a sequence of heating and cooling can be performed. Not all alloys can be heat-treated, as seen in table 2.1. Heat-treatable alloys are characterized by phase diagrams such as

that shown in figure 2.5. There are 3 main steps in the heat treatment. First there is solid solution heat treatment at a temperature above the solvus line (the lower leftmost line in fig. 2.5), which consist of a single phase α. The temperature are preferably below the eutectic temperature(548°C in fig. 2.5), to avoid melting. Then the metal is quenched down to room temperature, which places us in the two-phase region below the eutectic temperature and solvus line. Then the alloy will be in a saturated state. Then finally there is performed heat treatment at an intermediate temperature, typically 150-250 °C. This is called aging. In this section these steps be looked more thoroughly into.
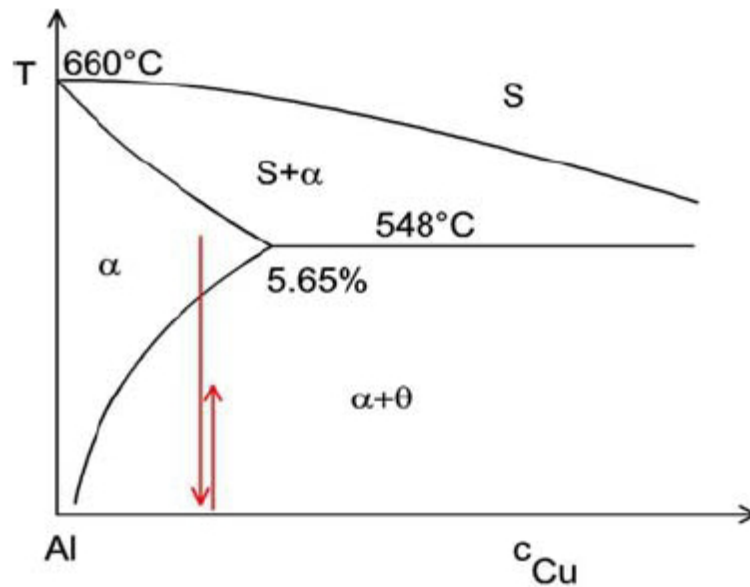

Figure 2.5: Al-Cu phase diagram.

2.5.1   Solution heat treatment (SHT)

The solution heat treatment has two purposes. Firstly, an alloy will not have a homogenous concentration of alloying elements after solidification. In order to produce a homogenous solid all the solute has to dissolve into the matrix of the metal. The temperature is chosen in order to get a high solubility. In figure 2.5 this can be understood by looking at the maximum fraction of Cu allowed in the pure α phase. This is given by the solvus line, and highest at the eutectic temperature. The time it takes to dissolve the solute varies with the diffusion speed. The holding time is typically 30 min to 1 hr.

The other reason for solution heat treatment is to introduce a large amount of vacancies. The equilibrium concentration of vacancies is given by [10]:

$$C_v = C_0 e^{-\frac{E_v}{kT}} \tag{2.2}$$

where C_0 is a constant, E_v is the energy required to introduce a vacancy, k is Boltzmann's constant and T is temperature in the Kelvin. There can be seen from the expression that the vacancy concentration increases exponentially with

temperature. Vacancies increase diffusion speed in the matrix, needed for the homogenization.

2.5.2   Super Saturated Solid Solution (SSSS)

A shown in the previous section, where equilibrium vacancy concentration will be relatively high at the solution treatment temperature. When the alloy is rapidly quenched from the high temperature there will be no time for a new equilibrium concentration to be established, and the high vacancy concentration becomes quenched in. Similarly the alloying elements are also quenched into the positions of the pure metal phase. This state is called a Super Saturated Solid Solution(SSSS). This condition creates a driving force for precipitation of a second phase since the temperature and solute fraction demands the two-phase region in the phase diagram. This means that the state is not in equilibrium e.g it is an unstable state. Therefore the intermediate storage time before aging is important, but will not discussed further here.

2.5.3   Aging

Finally, the alloy is aged and there is precipitation in the matrix. This is where the hardening effect comes from [3]. The selected temperatures and time determines which particles that will precipitate. When the microstructure gives the highest hardness, we have what is called the T6 condition. The aging is normally stopped at this point, by quenching. The precipitation sequence will be discussed further in a section below.

2.5.4   Overaging (OA)

If the alloy is heat treated after it has reached peak hardness, the precipitates will have less hardening effect since they are approaching the equilibrium phase. This is because these precipitates are incoherent. When this happens, it is called **overaging**. The precipitates that are present during overaging will be discussed in detail later.

2.5.5   Room temperature storage

The storage time that the alloy is kept at room temperature prior to aging strongly affect the nucleation of precipitates and may significantly change the number density [11]. Therefore it is important to have control over this event e.g by immediately start the ageing after the SSSS.

The storage time at room temperature after aging is not important. This is because the precipitates formed after aging will not transform at room temperature. This is indicated below in the phase diagram in figure 2.6 where the early formed precipitates (GP- zones) have a solvus line with lower temperatures.

2.6   Precipitation

Precipitates can be formed from nucleation and growth of particles containing solute atoms. The phases can be other than the ones depicted in the phase diagram. A phase diagram only gives the equilibrium phases. Other phases can also be very important because the phase-transitions discussed are diffusional transformations requiring a high vacancy concentration and thus high temperatures to occur in a reasonable time. This means that if a non equilibrium state is present at room temperature, the transformation time to the equilibrium state is very large. Such long lived phases are called metastable . Even tough the volume energy of the phase is higher, the total activation energy for nucleation can be lower for other configurations than the equilibrium phase. A phase diagram that includes metastable phases is depicted below in figure 2.6. All hardening phases are metastable.
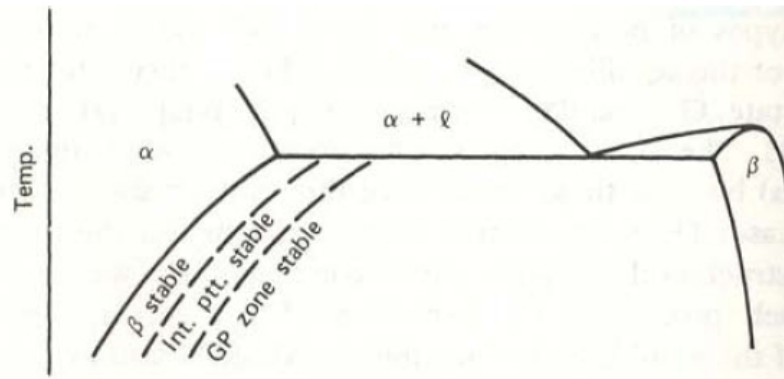

Figure 2.6: A metastable phase diagram [12] where some non- equilibrium phases are included. The metastable phases are indicated by the non- solid lines.

2.6.1   Homogenous nucleation

Consider figure 2.5 again. Assume that the α phase is Al-rich and that the θ phase is Cu-rich. Then we will have precipitation of θ from a supersaturated α solid solution. This involves two steps:

   I Cu-atoms within the α-matrix must diffuse together to form a small volume with the θ composition.

   II And then, if necessary, the atoms must rearrange into the θ crystal structure.

   The change in free energy during nucleation will be given by [10]

$$\Delta G = -V\Delta G_v + A\gamma + V\Delta G_s \qquad (2.3)$$

   where V and a is the volume and the area of the precipitate, respectively, ΔG_v is change in free energy per unit volume, γ is the interface energy per unit area and ΔG_s is free energy per unit volume due to misfit strain.

   The reason for the negative sign in front of the volume energy is of course that the final phase has lower energy than the SSSS. The origin of the second term is

the fact that a boundary is created along with the new particle. Thus the energy is positive because the boundary was not there before. The third term is because of the possible misfit between the particle and the matrix, as discussed in section 2.2.2. Assuming spherical particles gives

$$\Delta G = -\frac{4}{3}\pi r^3 (\Delta G_v - \Delta G_s) + 4\pi r^2 \gamma + V\Delta G_s \tag{2.4}$$

Minimizing eq. 2.8 gives

$$r* = \frac{2\gamma}{(\Delta G_v - \Delta G_s)} \tag{2.5}$$

and

$$\Delta G* = \frac{16\pi\gamma^3}{(\Delta G_v - \Delta G_s)^2} \tag{2.6}$$

The different terms are plotted in figure 2.7. It can be seen from the figure that if r < r* the system can lower its free energy by decreasing the radius. This means that it can dissolve the potentially new precipitates . Such unstable particles are called clusters. But if r > r* the free energy decreases by increasing r, thus the particle is stable and will grow. A stable particles is called a nucleus, and then with r > r* the criterion for **nucleation** is met. $\Delta G*$ is the activation energy for the nucleus to form.

Notice that the process above considers nucleation in the matrix. The particles can also reduce the free energy further by growing on crystal imperfections such as grain boundaries and dislocations, since the growing of a nucleus will result in destruction of a defect with higher energy than the matrix. This is called **heterogenous nucleation** [10].
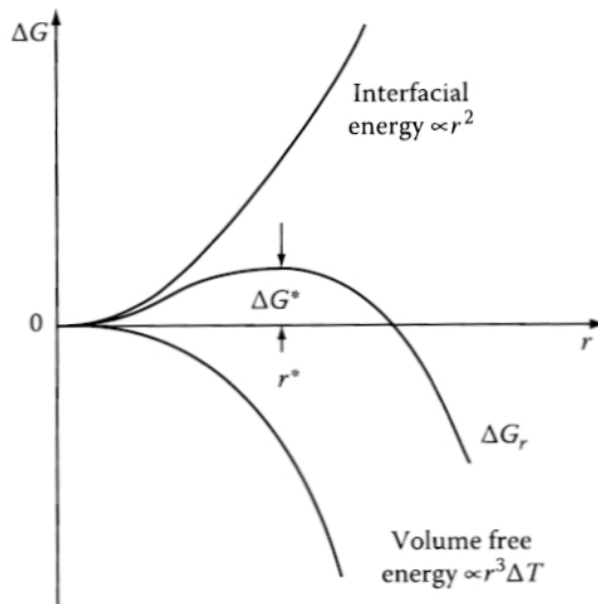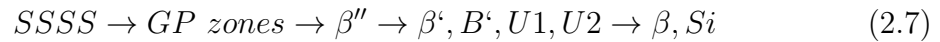

Figure 2.7: The variation of ΔG with r for a homogenous nucleus [10].

2.6.2   Precipitation sequence in Al-Mg-Si alloys

The formation of Al-Mg-Si alloys is done by adding a total amount up to 2wt% Mg and Si solute [13]. As a result of a similar heat treatment mentioned in section 2.5, the precipitation sequence will be [14],[15]

$$SSSS \rightarrow GP \ zones \rightarrow \beta'' \rightarrow \beta', B', U1, U2 \rightarrow \beta, Si \qquad (2.7)$$

All the phases given above except the two last are metastable, and will not occur in the phase diagram, as mentioned in the beginning of section 2.6. The phase diagram of Al-Mg-Si would be a 3-dimensional diagram and is therefore not included.

GP zones

The formation of a precipitate from a homogenous distribution of solute has to start with two solute atoms clustering together. A small number of atoms together is called an atomic cluster. When a cluster continues to grow from a random distribution of solute it will grow into a GP-zone. The GP zones are described in the literature as coherent and solute rich, spherical precipitates which are the first precipitates formed during aging [10]. Due to the coherency they will have low interfacial energy, and the activation energy for nucleation becomes smaller than for the equilibrium phase. These are expected to be observed in age-hardenable metals. In an Al-Mg-Si alloy (6082) it was found that the GP-zones are needle like [16].

β'' precipitates

These precipitate gives the main hardening effect in Al-Mg-Si alloys [3]. It has a needle like shape and is elongated along the $< 100 >_{Al}$ direction with a size of 4x4x50 nm [17]. It grows coherently along this direction, and semi-coherently in the two other directions. These precipitates appear when Al-Mg-Si alloys are heat treated between 125°C and 220°C, depending on the composition.

The crystal structure of the β'' precipitate is monoclinic with a = 1.516 nm, b = 0.405 nm, c = 0.674 and $\beta = 105.3°$. The composition is believed to be $Mg_5Al_2Si_4$ [18]. The angle between the β'' a-vector and $[010]_{Al}$ is 33.69° and the angle between the β'' c-vector and $[100]_{Al}$ is 18.43° [17].

Post-β'' phases

The precipitates formed after β'' give less strength to the alloy. They are formed during OA at a higher temperatures, and/or long OA times [11]. These post -β'' precipitates are characterized by a hexagonal configuration of a Si network found in the precipitates ([19], [20]). This can be used to identify them easily by considering a fast fourier transform of a precipitate phase.

I   The first overaged precipitate is called β' and does also grow coherently along the $< 100 >_{Al}$ direction [11]. These have a rod-shape and are much bigger, typically 20 x 20 x 500 nm [11]. It has a hexagonal unit cell with a = 0.705 nm and c = 0.405 nm.

II The three next considered is the U1,U2 and B' phases. These coexists with β' in the microstructure [11]. As with other metastable phases, these also grow coherently in the $< 100 >_{Al}$ direction.

- U1 is rod shaped and is most commonly observed in alloys with excess Si. It is trigonal with lattice parameters a = b = 0.405 nm, c = 0.674 nm , $\gamma = 120°$, and it has composition $MgAl_2Si_2$ [19].

- The rod shaped U2 phase is orthorhombic with a = 0.675 nm, b = 0.405 and c = 0.794 and composition given as MgAlSi [15].

- Finally we consider the B' phase. It has a rod or plate shape and is found to grow on dislocations [11]. Composition is unknown, but it has been observed to be hexagonal with lattice parameters a = 1.04 nm, c = 0.405 nm and $\gamma = 120°$.

2.6.3   Industrial alloys

Other elements like Mn and Fe can also be added in small amounts along with Mg and Si without changing the precipitate sequence, but for grain size control [13]. The alloy is then called an industrial alloy. The mechanism which the controlling of the grain size occurs is by creating particles that influence grain growth. These particles are called dispersoids, and are bigger than the other precipitates. But for a given alloy with same treatment the grain size is constant and this will not be discussed further here.

2.7   Transmission electron microscopy

A TEM works similar to an ordinary light microscope, but there are some major differences. The TEM uses electrons instead of light for observing the specimen, and the refractive medium controlling the light is replaced by magnetic lenses. Electrons interact strongly with matter, and the components interacting with them are therefore placed in a vacuum. The Rayleigh criterion states that the smallest observable feature in an optical microscope is limited by the wavelength of light:

$$R = \frac{0.61\lambda}{\mu sin\beta} \tag{2.8}$$

where λ is the wavelength of light, μ defines the viewing medium and β is related to the depiction device. The important part is that the resolution is proportional to the wavelength. By changing radiation from light to electrons, the wavelength is no longer the limitation, and the resolution can be increased dramatically. The best light microscopes have a resolution of 200 nm, while a good TEM has a 0.1 nm resolution. Materials have an interatomic length in the same order of magnitude , and can therefore be observed with a TEM.

Figure 2.8: A Philips CM30 TEM operated by my supervisor Calin D. Marioara. Notice the vertical column where all the important components are placed.

2.7.1   Main components of a TEM

As mentioned above the TEM works similar to the light microscope. The light image is determined by how much of the light that gets through the different sample areas, while the TEM image is produced from electrons going through the specimen. This is why very thin samples are required. Since the lenses are magnetic, their strength can be easily controlled by varying the current that creates them. This allows the TEM to easily switch between different modes. A very useful property of the TEM is that it can be operated in diffraction mode due to the short wavelength of electrons. This means that also crystallographic investigations can be performed just by varying the strength of the magnetic lenses.
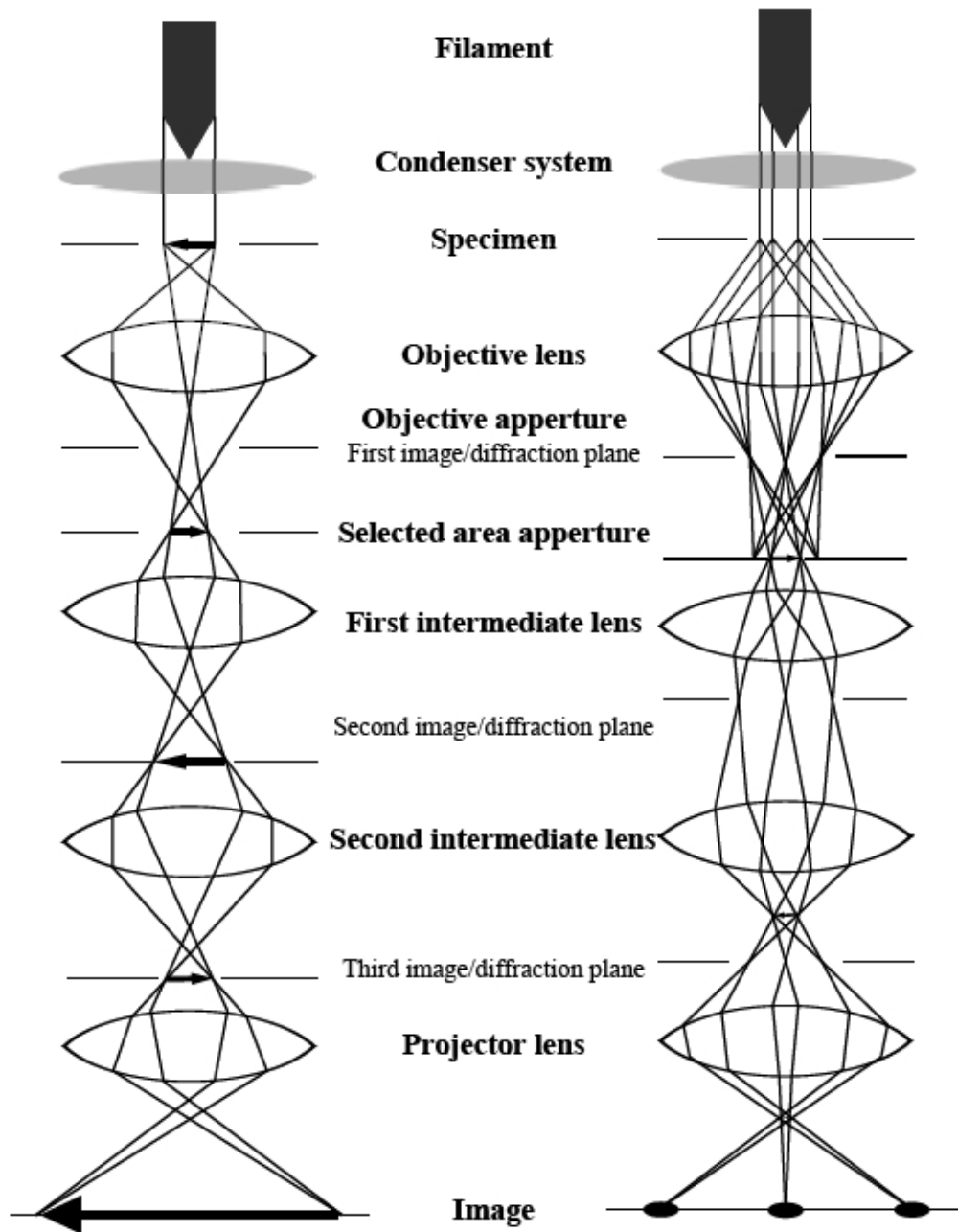
Filament

Condenser system

Specimen

Objective lens

Objective apperture
First image/diffraction plane

Selected area apperture

First intermediate lens

Second image/diffraction plane

Second intermediate lens

Third image/diffraction plane

Projector lens

Image

Figure 2.9: A schematic drawing [8] showing a TEM in both diffraction mode (right) and imaging mode (left).

A drawing of the components in a TEM i shown above in figure 2.9. Starting from the top:

- At the top there is an electron source. This is called the **electron gun**. There are two main types of electron guns: field emission gun (FEG) and thermionic source. The thermionic source works by heating a filament until it emits electrons. There are two types of filaments: Tungsten and LaB_6. Tungsten filaments have higher energy spread, lower brightness and lifetime than LaB_6, but require a lower vacuum. The FEG works by emitting electrons through a thin tip due to a electric field. This results is a more coherent beam but

requires an even higher vacuum.

- Below the electron gun is the **condenser system**. This is a set of electro-magnetic lenses which focuses the electron beam on the specimen. It controls the size of the electron probe.

- The electron probe created in the previous step sends electrons through the specimen which is placed right below.

- Located near the specimen is the **objective lens**. This is the most important lens in the TEM. This is because it forms the images (seen on the left side of figure 2.9) and the diffraction patterns (seen on the right side of figure 2.9).

- The rest of the components are only used to magnify and obtain the images formed by the objective lens.

- In addition to these components there are apertures, which are devices that physically block part of the electron beam. These also keep the electron beam close to the optical axis(which is the imaginary line down the column of a TEM) , because the errors made by the lenses get larger away from the axis.

When an aperture is inserted in the back focal plane of the TEM, choosing only the direct beam in the diffraction pattern , we do bright field imaging. This is illustrated below in figure 2.10. The scattered electrons are not part of the image formed. A dark field image is formed by choosing one of the diffracted beams.
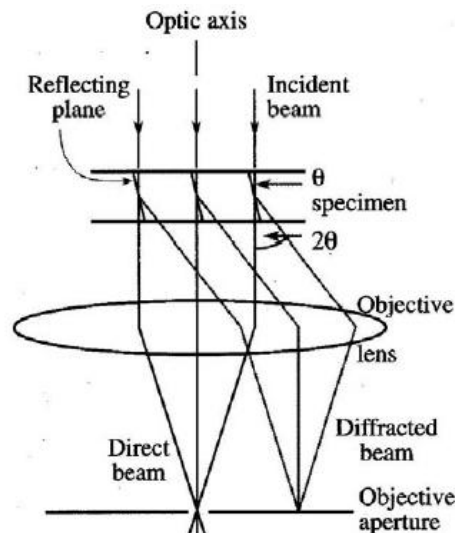

Figure 2.10: A TEM operating in bright field mode [21].
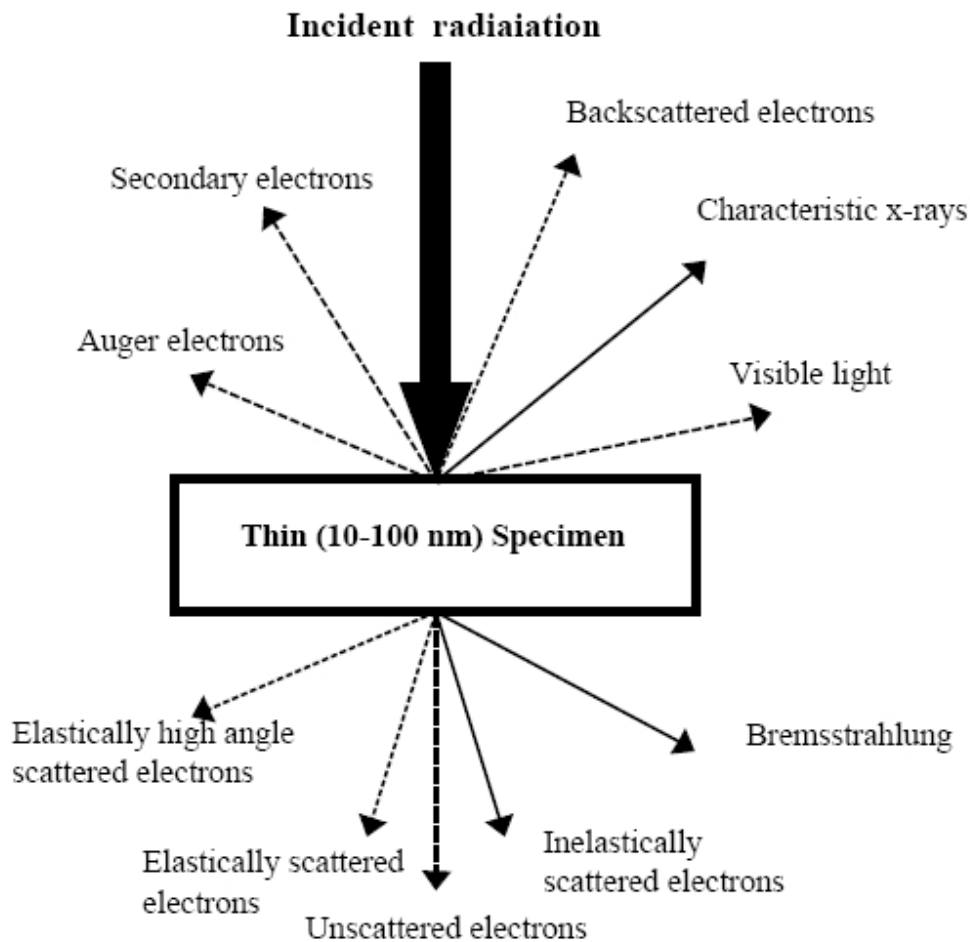
2.7.2   Scattered electrons and diffraction

Figure 2.11: An illustration [8] of different signals generated when the electrons hit the sample.

When the electron beam hits the sample there can be many outcomes. In this thesis the direct unscattered beam was used to create a bright field image, as discussed under the aperture point in section 2.7.1. In addition, the inelastically scattered electrons were used for Electron Energy Loss Spectroscopy (EELS), as discussed below. Some other outcomes are depicted in figure 2.11.

Phase contrast

Electrons scattered away from the optical axis will pass through the optical lenses similar to the unscattered electrons, but they travel a small distance from the axis. When the electrons reach the final image they have traveled a longer distance than the unscattered electrons, which leads to a phase shift. This can lead to interference in the image. This effect is called **phase contrast**. Phase contrast is important on high resolution TEM, but has a very small effect at low magnification [22].

Diffraction

When the electrons are scattered the amplitudes on the outgoing waves depend on the difference in path length. For constructive interference to occur, Bragg's law has to be fulfilled:

$$2dsin\theta = n\lambda \tag{2.9}$$

where λ is the wavelength, d is the distance between atomic planes, 2θ is the difference between incoming and outgoing wave, and n is an integer. The derivation is illustrated below in figure 2.12.
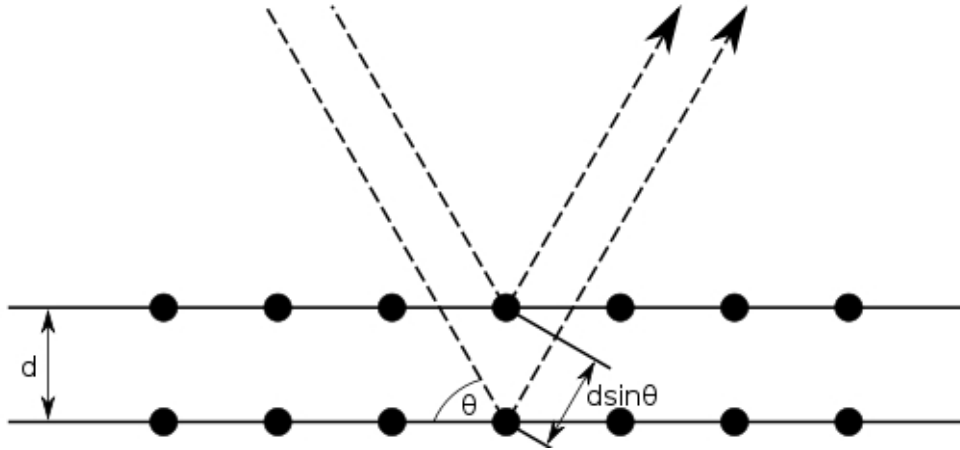

Figure 2.12: Bragg diffraction [23]. Two beams with identical wavelength and phase approach a crystalline solid and are scattered off two different atoms within it. The lower beam traverses an extra length of 2dsinθ. Constructive interference occurs when this length is equal to an integer multiple of the wavelength of the radiation.

The right side of Bragg's law measures the number of wavelengths that fits between two rows of atoms, thus measuring reciprocal distances. Reciprocal lattice vectors describe the set of planes as a normal vector to the planes, with length G = $2\pi/d$. Bragg diffraction of electrons in crystal occur when [21] :

$$\vec{G} = \Delta\vec{k} \tag{2.10}$$

where $\vec{G}$ is a reciprocal lattice vector and $\Delta\vec{k}$ is the difference between the incoming and outgoing beam. This is called the Laue criterion. In order to visualize this, the reciprocal lattice together with the beams is drawn in what is called an Ewald construction, shown below in figure 2.13. A sphere with radius given by the length of the incoming wavevector is drawn. If it intersects a reciprocal lattice point the Laue criterion is fulfilled. Due to the $1/\lambda$ dependance of the radius and small wavelength of the electron a large ewald sphere and thus many diffraction spots can be seen at once in the diffraction pattern.
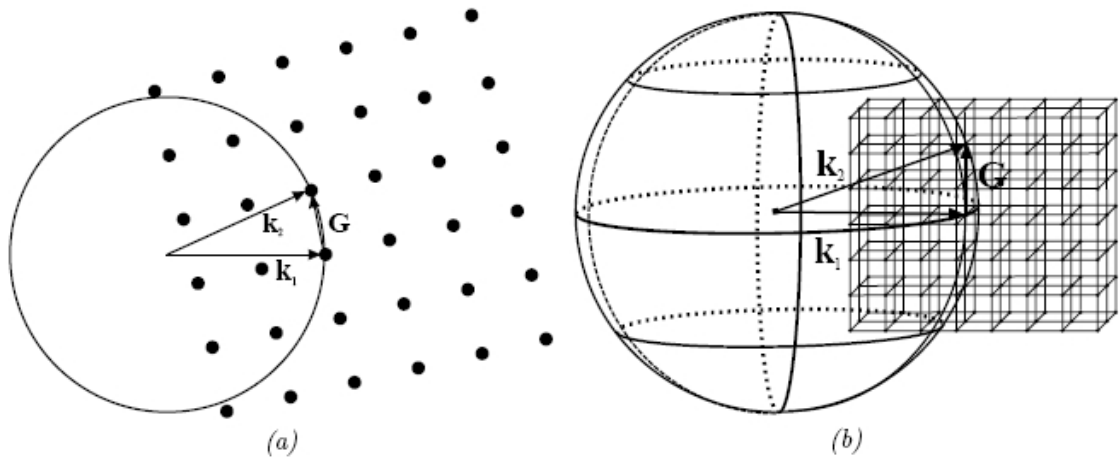
Figure 2.13: Ewald construction [8] in two (a) and three (b) dimensions. Notice that the radius of the sphere should be given by $2\pi/\lambda$.

2.7.3   Electron Energy Loss Spectrum

As mentioned above in section 2.7.2 some of the electrons going through the sample will be inelastically scattered. Together with the unscattered electrons, the energy spectrum for all these electrons can be used to find, among another things, the thickness of the sample. It is very important to obtain the thickness of the sample when statistics are collected. For example if the number density of precipitates is counted from TEM images, the thickness is needed to calculate the volume of the counting area.
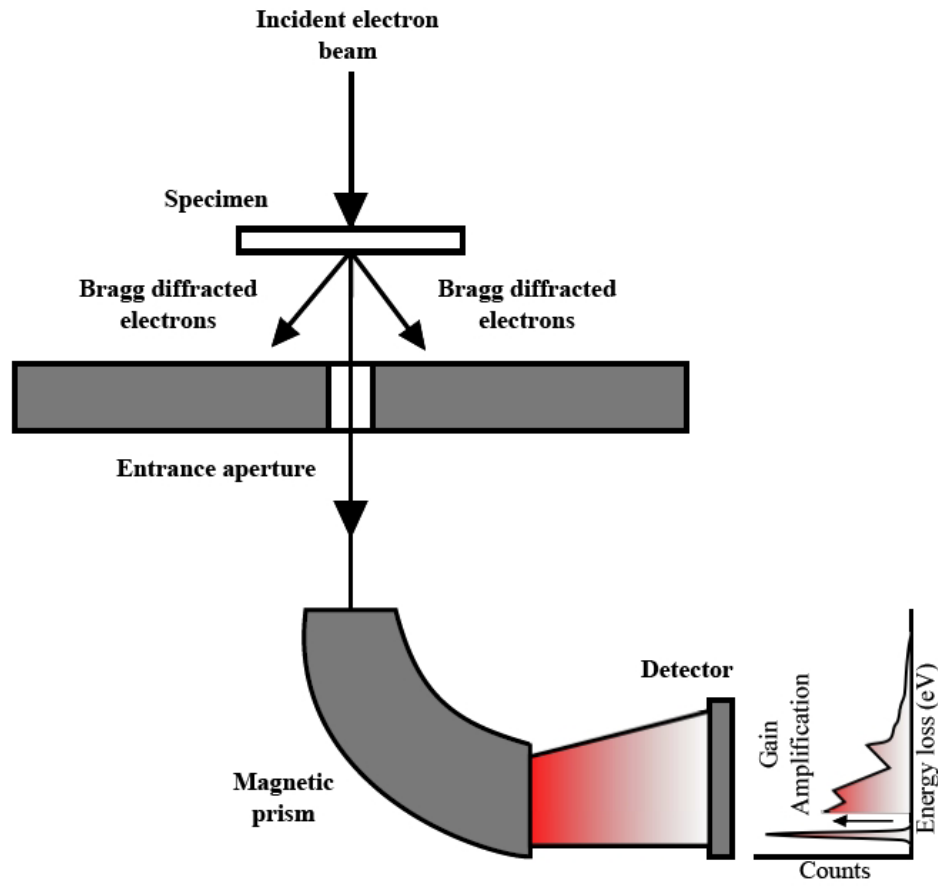
Figure 2.14: A schematic overview of an EELS module [24]. Unwanted electrons are removed by the aperture, and the rest are deflected according to their energy. Then they are detected and the counts in the detector produces an energy spectrum. Notice the zero-loss peak , which has the highest number of counts.

The spectrum is obtained by a simple method. All electrons will be sent through an aperture that lets through only the unscattered and forward inelastically scattered electrons, see figure 2.14 above. Then, with use of a electromagnetic prism, the electrons will be deflected differently depending on their energy according to the Lorentz force

$$\mathbf{F}_{mag} = Q(\mathbf{v} \times \mathbf{B}) \tag{2.11}$$

where $\mathbf{F}_{mag}$ is the magnetic force, Q is the charge of the electron, $\mathbf{v}$ is the velocity of the electron and $\mathbf{B}$ is the magnetic field.

The electrons having lost no energy will be less deflected than the ones having lost energy to the sample. Since the inelastically scattered electrons will be bent more they make up the rightmost part of the spectrum in figure 2.14. With a thin sample, most of the electrons will pass through the material without loosing any energy, and these electrons will correspond to the zero-loss peak (ZLP) in the energy spectrum. The following peaks are called the plasmon peaks. They are due to collective oscillations of free electrons that occur when a beam electron interacts

with the free electrons gas [21].

Since the electrons can be shown to have a mean free path, it can be used to calculate the thickness of the sample. The plasmons are a result of that the atomic lattice is struck by a beam electron [21]. The number of unscattered electrons are also known. If there is assumed that the sample is thin enough so that only one plasmon interaction is allowed per electron, the ratio between the low loss area (total intensity between 0 and 50 eV) and the ZLP can be used to calculate the thickness:

$$t = \lambda \frac{I_1}{I_0} \tag{2.12}$$

where t is the thickness of the sample, λ is the mean free path, I_1 is the intensity of the low loss area and I_0 is the intensity of the ZLP.

Chapter 3

Experimental

3.1 Alloy and pre-treatment

In this thesis all experiments have been done with the same alloy. The alloy is an industrial 6060 alloy with composition(wt%) 0.45Si, 0.37Mg, 0.20Fe, 0.02Mn and the rest is Al. The alloy was extruded into long bars with circular profiles of 2 cm diameter. The extrusion direction was indicated with an arrow on the bar. The reason for using only one alloy composition is that the alloy will be given different heat-treatments. As discussed above, the properties of the material will depend strongly on how it is heat treated.

Before heat treatment a bar 90 cm long was cut off and then divided into 3 bars with length 30 cm each. These will be heat-treated differently. The bars were cut with a Struers Discotom 2 machine. Two of the bars were cut into three bars of length 10 cm and solution heat treated and aged, before they were cut again into 15 bars of 2 cm length. The last bar was cut into 15 bars before solution heat treatment.

In order to heat the small cylinders in an efficient way, holes were drilled into the samples. The holes were drilled straight down parallel to the axis of the cylinder, and to the side. There was used a 2.5 mm twist drill. The drill can easily break if it is thinner than this. Even at this size there can be problems. There was experienced that if the resistance during drilling suddenly increased, the drill should then be cleaned of aluminium fillings before continuing.

Each of the small cylinders was marked with a diamond-tip pen.

3.2 Heat treatment (HT)

The heat treatment is divided into three steps. Solution heat treatment, aging and overaging. The first and the last step are the same for all three bars. For the last bar aging and overaging is combined into the same treatment. The three bars was heat treated with the following three different procedures:

I **Heat treatment 1 (HT1)**. The first bar was given **SHT** at 530°C for 10 minutes in a salt bath. Afterwards it was quenched down to room temperature.

Then immediately followed by **aging** in an air-circulation furnace. First the bar was heated 3.33°C/min up to 150°C, immediately followed by 0.33°C/min to 195 °C. Then it was hold at 195 °C for 150 min. After aging it was quenched down to room temperature. The HT is illustrated in figure 3.1. This treatment should give a few large β" precipitates compared to HT2. This is because of the higher temperature gradient in HT1. There is less time do develop nucleation sites such as clusters and GP-zones for the β'' particles, leading to fewer and larger precipitates. After aging the sample was stored at room temperature, but as mentioned above this should not influence it.
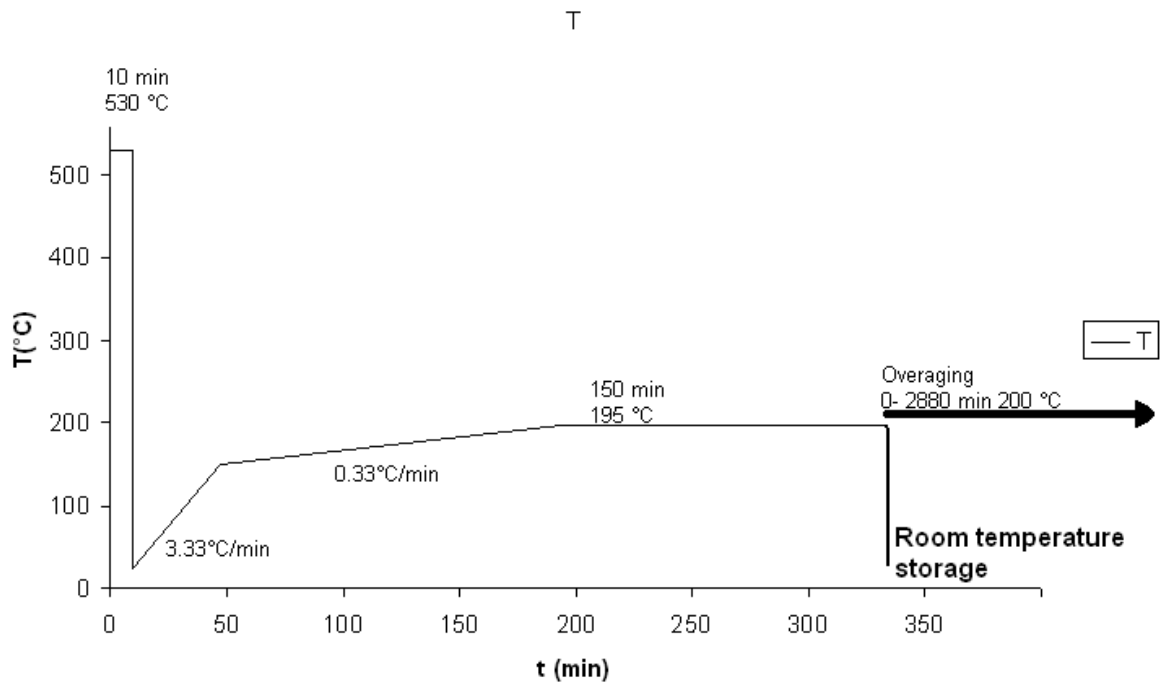
Figure 3.1: SHT, aging and overaging for the first bar.

Finally the alloy is cut into 15 small bars where 1 is kept as a starting condition for **overaging**. The remaining 14 bars will be heat treated in an oil bath at 200°C for various times, each of them representing an overaged condition. The overaging times were:

- 10min / 20min / 40min / 60min / 90min / 120min / 180min / 270min / 330min / 420min / 600min / 960min / 1440min / 2880min.

II **Heat treatment 2 (HT2)**.The second bar was given **SHT** at 530°C for 10 minutes in a salt bath. Afterwards it was quenched down to room temperature. Then immediately followed by **aging** in the air-circulation furnace. First the bar was heated 0.33°C/min up to 195°C. Then it was hold at 195 °C for 150 min. After aging it was quenched down to room temperature. The HT is illustrated in figure 3.2. This treatment should give many small β" precipitates compared to HT1, for the same reason discussed under HT1. After aging the sample was stored at room temperature.
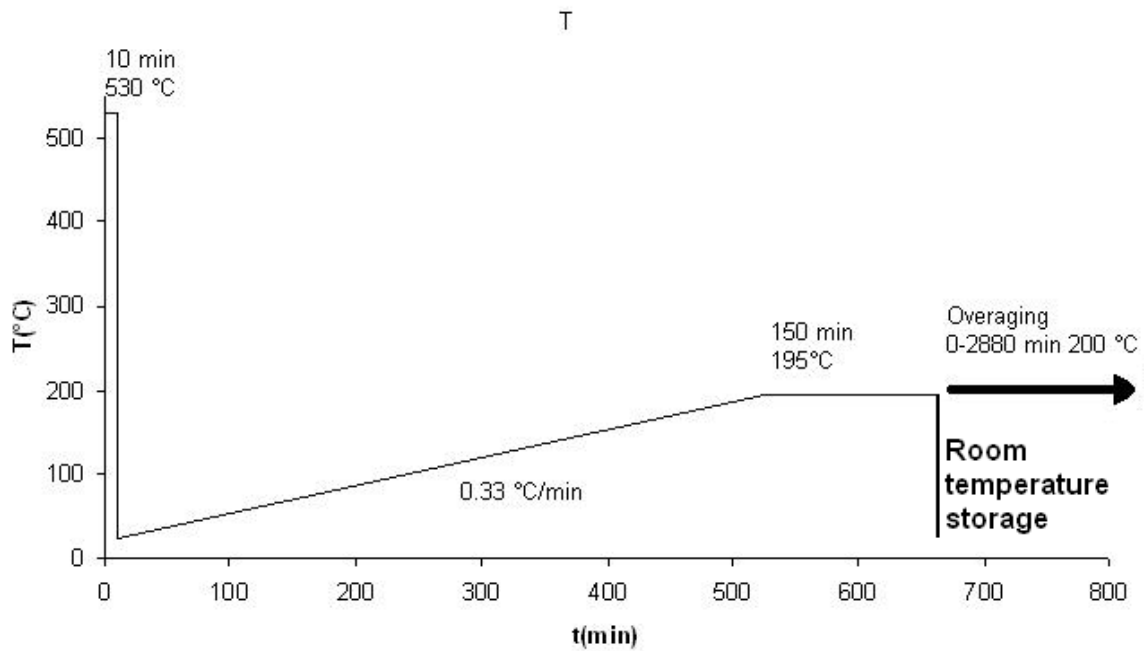
Figure 3.2: SHT, aging and overaging for the second bar.

Then it was **overaged** in the same way for the same times as the first bar.

III **Heat treatment 3 (HT3)** The third bar was given **SHT** at 530°C for 10
minutes. Then it was quenched down to room temperature, immediately fol-
lowed by the overaging treatment given to the first two bars. This means that
the alloy will be aged and overaged in the oil bath. For this treatment the
whole range of hardening conditions from SHT increasing to T6 and then de-
creasing towards the equilibrium phase will be obtained. This HT is illustrated
in figure 3.3 below.
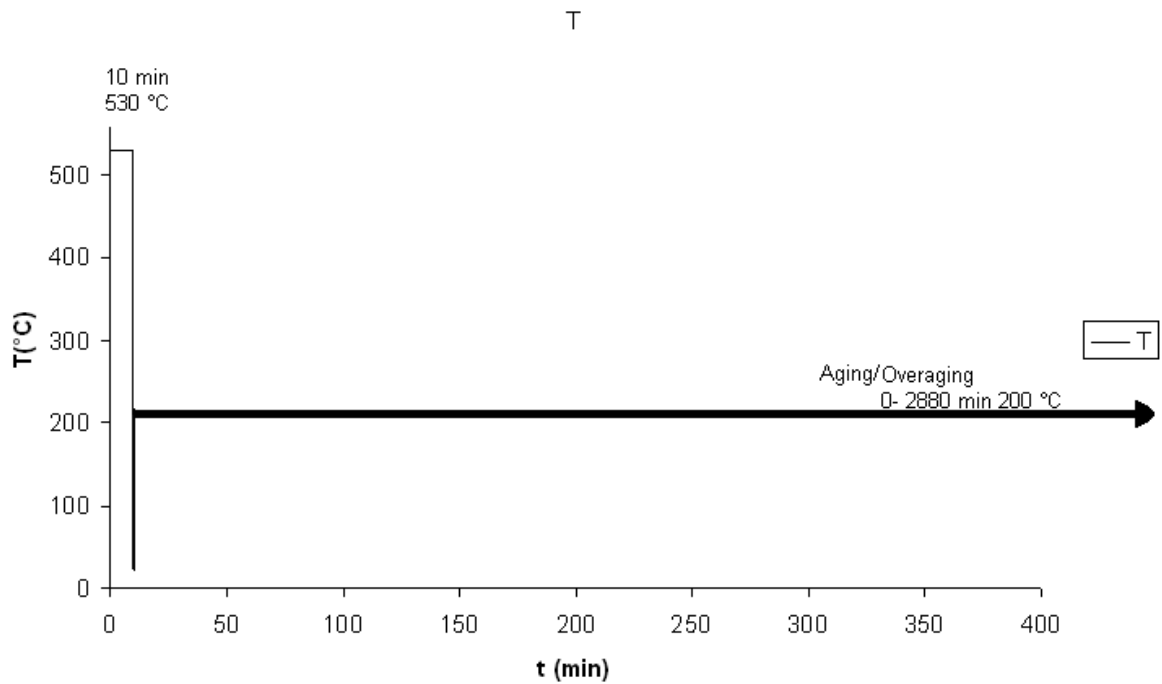
Figure 3.3: SHT, aging and overaging for the third bar. Notice that aging starts immediately after SSSS and is combined with the overaging at the same temperature of 200°C.

3.2.1   Temperature stability

The temperature reliability during SHT, aging and OA were investigated.

The temperature in the salt bath dropped approximately 10°C when 3 cylinders with r = 1 cm and h = 10 cm were solution heat treated. This is because the alloy was at RT and would cool the salt bath. But after a few minutes the temperature was back to 530°C.

The time between water quench after salt bath and the heat furnace was about 30 seconds, because the sample had to be properly aligned in the oven so that it would be heated approximately homogenously. In order to check the temperature at the sample during aging in the oven, a temperature logger was used. The results are shown below in figures 3.4 and 3.5 for HT1 and HT2 respectively.
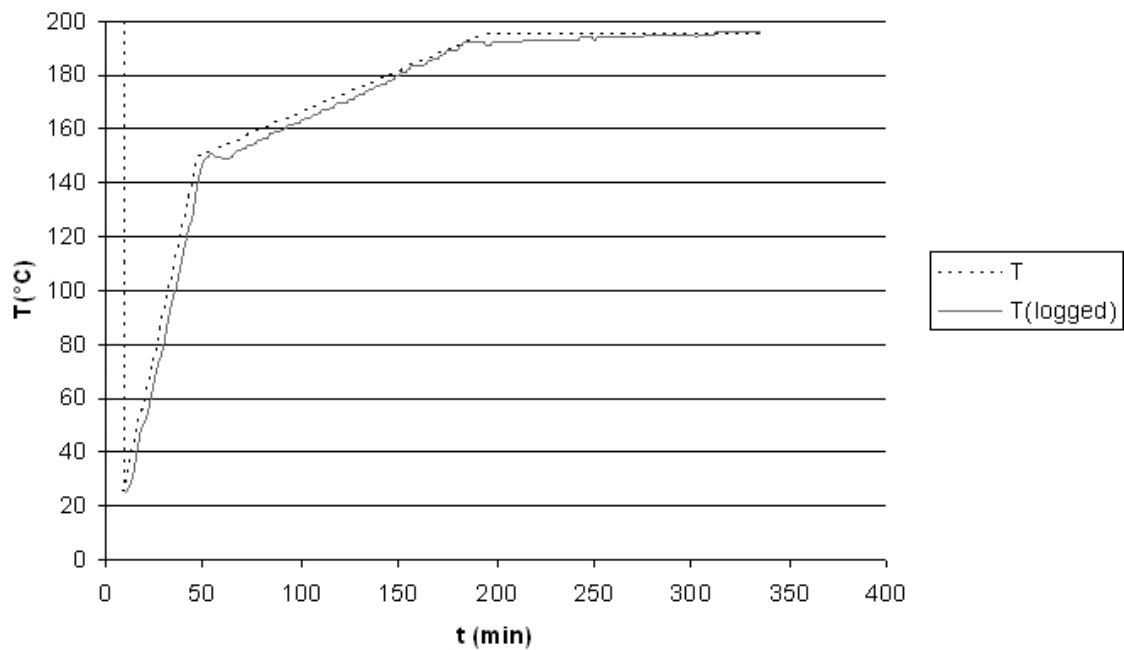
Figure 3.4: Temperature logging for the aging in HT1 done in a heat furnace. T is the preprogrammed temperature, and T(logged) is the temperature recorded by a thermometer at the sample.
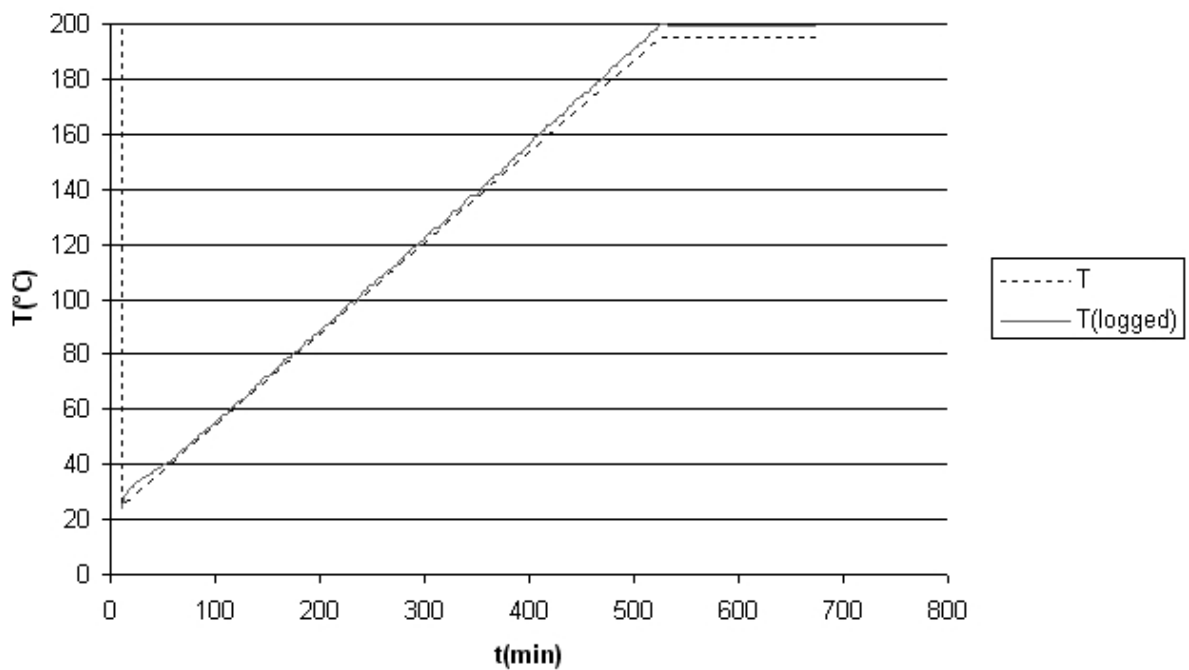

Figure 3.5: Temperature logging for the aging in HT2 done in a heat furnace.

A couple of spot tests were made of the temperature in the oil bath during OA, and all were between 198-200 °C. There was a small drop in temperature after the samples were added in the oil bath, but after 4 minutes it had increased to 200°C.

3.3   Hardness measurements

The hardness measurements were done using a Struers Duramin A-2500, shown in figure 3.6. Hardness were measured on both sides of the cylinders. There was made 5 indentations on each side. The indentations were made 2mm away from the center and 3 mm away from the edge of the samples which have a 2 cm diameter. The load used to make the indentations was 1 kg. The load was selected based on the size of the indentation. The size should be large enough to get good readings, but it cannot be larger than the area limited by the camera used to get an image of the indentation. Using a screen and a control panel below, as seen in figure 3.6, the corners on the indentation were marked, and also the diagonals. When these were selected, the hardness was automatically calculated and the hardness value could be obtained from the screen. Then the average of 10 indentations + standard error was calculated.

Figure 3.6: The Struers Duramin A-2500 used for hardness measurements.

In order to get a flat and clear surface, the cylinders were polished with SiC papers up 1200pp, were increased pp value means higher fineness. If the surface was not flat, the indentations would be very deformed. Such deformed indentations are strongly unwanted because the test is based on proper diagonals. Therefore a clip was used to hold the cylinder during polishing, in order to ensure that the top and bottom of the cylinder were approximately perpendicular to the cylinder axis.The clip is shown in figure 3.7. The polishing was also done in order to get a more shiny and smooth surface so that the corners of the indentation would be easier to observe.
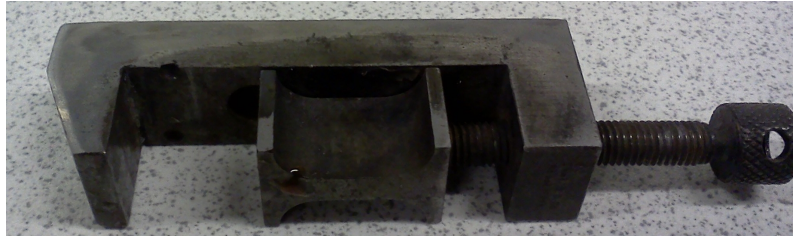
Figure 3.7: Clip used to hold the 2 cm bars during grinding.

3.4   TEM

In this work the microstructure of a few samples from HT1 will be examined, and based on the hardness curves the samples representing certain overaging times were selected.

3.4.1   Preparing the sample

In order to get good pictures in the TEM, the sample has to be thin and without contamination. During preparation there is no way to ensure that the sample is good, because other instruments can not check for faults at the same resolution. Below there is described a procedure of how to make aluminium TEM samples.

  I A disc with a thickness of approximately 2 mm was cutoff each of the selected samples, using the Struers Accutom 5. This was done because it would be extremely time consuming to grind it, and also because the number of final samples will increase as the disc thickness decreases. During this work it was not critical to get many samples from one cylinder, but if e.g all the OA times was done on the same cylinder, this would have been very important.

 II Then the samples were ground with SiC papers of fineness 600, 1200, 2400 and 4000pp. During grinding, the sample thickness was measured with a light microscope. This was done by first focusing on the topside edge of the sample, and then moving outside the sample. The distance the microscope was lowered in order to focus on the holder would then be the height of the sample. This was done on 4 equally separated points along the circumference in order to get a measure of the height differences and an average thickness. The thickness should not differ to much around the sample, because then it could be difficult to get an even thickness of about 80-120μm for the final disc.

III After the grinding, the thin disc was used to make smaller discs with a diameter of 3 mm. These were made using the device from Gatan shown in figure 3.8. These discs are of the size required to fit into a TEM sample holder. But first the sample had to be made much thinner.

Figure 3.8: Device used to make 3 mm discs.

IV The discs were then treated with a method called electropolishing. During electropolishing the metal in the middle of the sample is oxidized and dissolved in a electrolyte. Finally there would become a hole in the sample, and the area around the hole would be very thin. The electropolishing was done using a Struers Tenupol-5. The electrolyte that was used was 1/3 nitric acid and 2/3 methanol. It was cooled down to -30 to -20 °C using liquid nitrogen. The nitrogen had to be refilled about every 10-15 minutes in order to stay in the desired temperature range. Considering the time, this point was critical. If there was to much nitrogen the electrolyte would get too cold and solidify, and electropolishing could not be performed until the temperature had increased. Therefore it was important to add only small amounts of liquid nitrogen. There was a photo-sensor determining the size of the hole, and this was set to a value between 100 and 400. This value represent how much light that goes through the hole made in the sample, relative to no light (0). The flow rate was set to 38 and the voltage was 20 V.

3.4.2   The microscope

In this work there was used a Philips CM30 Transmission Electron Microscope. The electron source was a LaB_6, and it was operated at a high voltage of 150 kV. The pictures were taken at a high magnification of 340 kx. This was appropriate considering the size of the particles. A double tilt holder was used, which means that the sample can be tilted in two directions. On the CM30 the sample can be tilted 45° in one direction and 30° in the other. Another microscope with higher resolution was also used, but it was operated by my supervisor and will be discussed later.

3.4.3   Operating the microscope

In order to get a good TEM picture there are certain prerequisites.

- The sample has to be thin enough.

This is a general requirement when using a TEM, because if the sample is too thick, there will be no contrast. This might seem obvious, but in order to ensure that the sample is thin enough the objective aperture should be used, and centered on the brightest spot. This is in order to block out the contributions from the other spots in the diffraction pattern, and thus increasing the contrast. Assuming all alignments and settings are in order, there should now be possible to search for bright areas indicating a thin sample area, suited for further examination.

- The sample has to be aligned in the right direction.

This point has to be emphasized when working with aluminium because there is the possibility that you cannot align your sample in the preferred direction. For e.g a thin film sample, the interesting area is aligned beforehand when preparing the sample. The final alignment will then be small. In aluminium the grains are randomly aligned. The precipitates grow in the <100> directions [17] [25], making the cross sections visible when the electron beam is parallel to this axis. The zone can be found by maneuvering in the reciprocal space, and finding the bottom of an Ewald sphere with the right pattern. The diffraction pattern in the ¡100¿ directions is quadratic, as shown in figure 3.9.
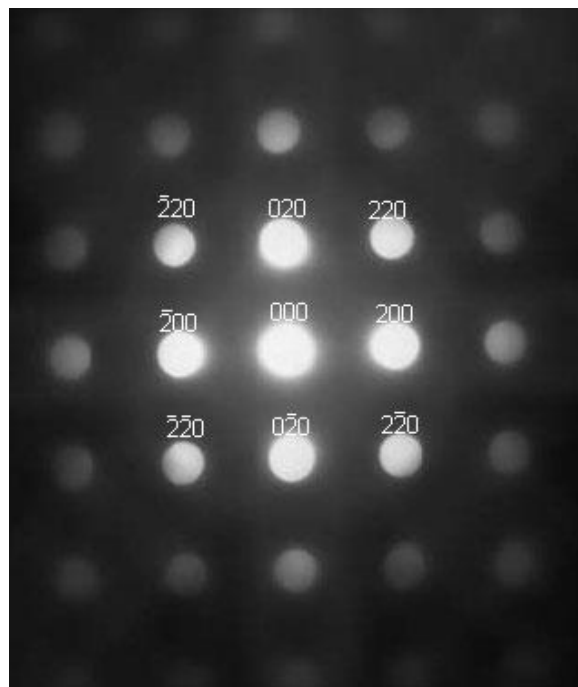

Figure 3.9: A TEM picture of the diffraction pattern along the [001] axis. The indices on the diffraction pattern are indicated.

If a <111> zone is found, it can be calculated from the fcc lattice that a tilt of 55° is required to get to the [100] direction. Similar the tilt is 45° from a <110> zone. This means that your [100] direction will not be found in this particular grain, because the tilt required is too large. Then a new grain has to be examined. This can mean that you have to change your sample, and that the current sample is of no use. That is why a large number of samples should be made when working with

aluminium in TEM, typically 10 samples per condition are sufficient. In this work there was made 10-20 samples on each condition.

3.4.4   High Resolution TEM (HRTEM)

In this work there was also used a Jeol 2010f high resolution transmission electron microscope (HRTEM). The magnification used was 1168 kx. This was operated by my supervisor Calin D. Marioara, and will therefore be discussed briefly here.

The microscope had a FEG electron gun operated at 200 kV. The voltage was fixed, so the electron energy could not be adjusted as with the CM30. This results in a beam damage on aluminium samples, and precipitates can be damaged in a time as short as 1 minute. This is important to notice when using this type of microscopes, in order to avoid that one specific area is imaged for a long time.

As mentioned in section 2.7.2 the effect of phase contrast will be visible at high resolution. The off axis electrons mentioned above that are needed to create the phase contrast are included by using a large (or no aperture) objective aperture. Small adjustments in the settings of the microscope that are affecting the phase contrast will make changes in the smallest details of the image, which makes it hard to know what is the "real" image. Therefore this kind of work needs some experience, and when there is known what to expect in the image, the settings are easier to adjust.

Fourier Transform Filtering

The HRTEM images were enhanced by using a software called Digital Micrograph. First a Fast Fourier transform was done of the picture. Then a function called BandpassMask was used to remove any spatial frequencies below 0.15 nm. Then an inverse FFT was performed. This removes unwanted noise.

3.4.5   Obtaining precipitate statistics

To get an overview over how the samples evolve during overaging, there were taken pictures to obtain cross section, length and number density of the samples. Due to variations in density the magnification varied between 31 kx and 89 kx in the low resolution images from the CM30. The number of images also varied due to the density, and there were used 3-6 images for the low resolution, giving between 900-1900 cross sections and 700-1100 needle lengths for the first four conditions. For the overaged conditions it was harder to obtain needle lengths and there was only used 430, and the number of cross sections was 1100. The high resolution images from the CM30 were at a magnification 492 kx, and at least 30 precipitates were used, from between 4 and 12 images. For the fourth TEM sample (OA of 600 minutes) 12 of the cross section sizes came from the HRTEM pictures taken with the 2010F, because there were only 18 cross sections with good quality from this sample from the 492 kx pictures. The average cross section sizes from the images by both CM30 and the 2010F turned out very similar, so this should not lead to any problems with the statistics.

All the pictures that where taken to get the number density had to be supplemented with EELS measurements obtaining the thickness. This was done because the TEM image is only a projection of the sample area, so the particles that is viewed will be at different heights in the actual sample. To calculate the density the volume is needed, and this will be given by the picture area times the thickness, assuming it does not vary over the picture area.

In addition to the measured quantities, the volume fraction of precipitates was also calculated. The volume fraction tells us how much of the volume investigated that contained precipitates. Since the average number density is obtained, and also the size of the particles (assuming volume = cross section × length), the volume fraction will be given by:

$$VF = \langle CS \rangle \cdot \langle \rho \rangle \cdot \langle l \rangle \qquad (3.1)$$

Counting procedure

The particles were counted using a software developed by Sigurd Wenner. The software measures the number of, length and cross section of colored continuous areas in a picture. Then the average and standard deviations of the above quantities are given as output. So if for example the number of cross sections and their size is to be obtained, this can be done by coloring the cross sections and giving the picture as input to the program. Then the number of cross sections, their average size and the standard deviation will be given. In order to find the length of the needles the [010] and [001] directions has to be counted separately to avoid overlapping of the colored areas. This is because the program counts each continuous area as one particle. Finally, to obtain the number of cross sections in a low resolution picture there is enough to just mark each particle with a dot so that each particle is counted. This is done because the size and length is of no interest when the number density is calculated. Below in figure 3.10 the coloring procedure for a low resolution picture is illustrated. After each picture was colored the original picture was deleted from the background in order to save disk space, so only the colored areas remains, as seen in the figure.
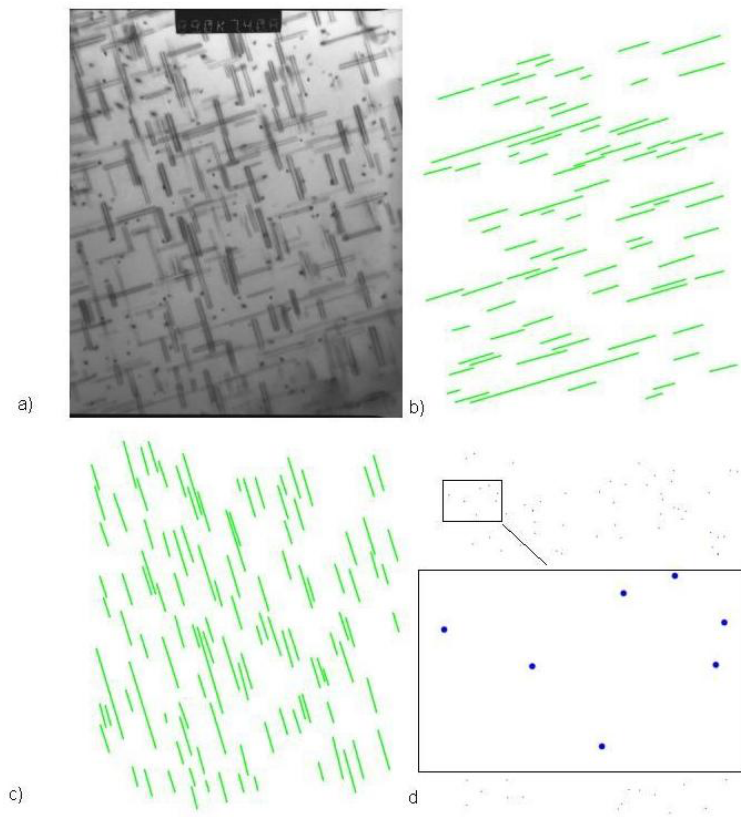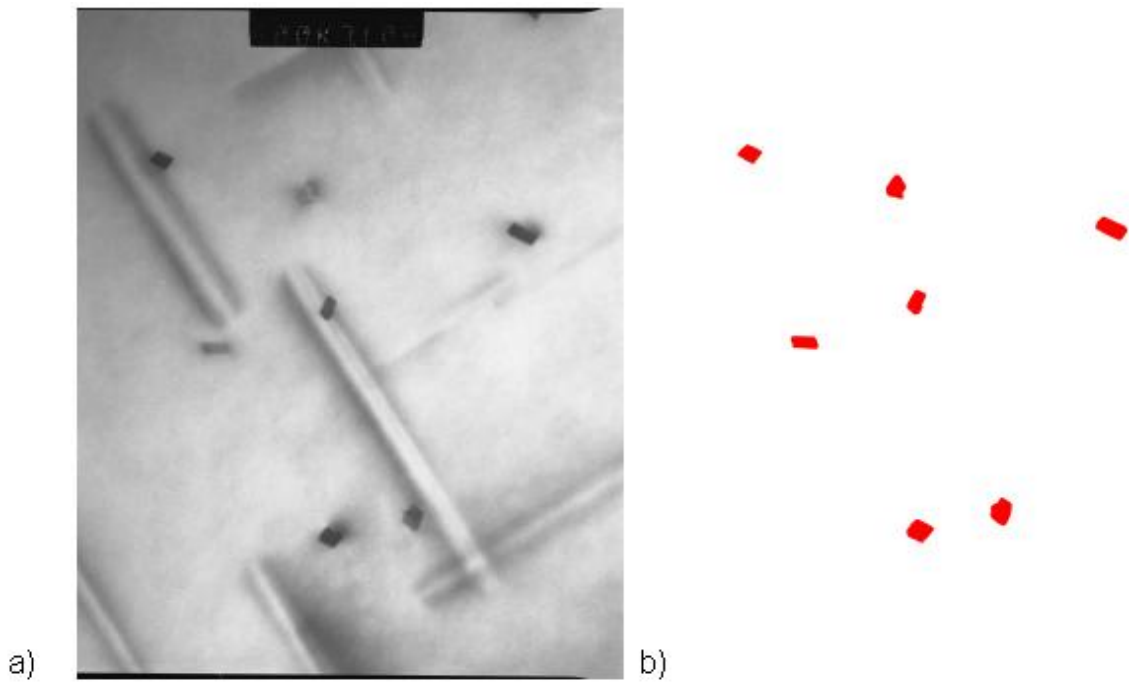
Figure 3.10: Coloring procedure for the statistics software at low resolution. a) shows the original picture. b) and c) shows the length measurement in the two orthogonal directions. d) shows the marking of particles for number density calculation. The dots are very small because the program only needed a small spot to make a count. Notice that the background (original picture) was deleted so that only the colored area was saved.

The coloring of cross sections is done at a much higher resolution than the number density and length. As it can be seen in figure 3.10 the cross sections used as statistics for the number density is very small, and the dots counting them can barely be seen. An example of a picture with higher resolution and a picture of the colored area feeded into the program is given below in figure 3.11

Figure 3.11: Coloring procedure for the statistics software at high resolution. a) shows the original picture. b) shows the colored area after the background is deleted.

Correction for length and number density

Both the needle length and the number density must be corrected after the numbers are obtained from the counting discussed above.

Firstly, the length of the needles must be corrected. The zone axis is often in another direction than the initial viewing direction with no tilt. Therefore the sample has to be tilted to find the [100] direction. As a result of this, some of the needles observed will actually be cut needles, and therefore appearing shorter than they really are. This will give an underestimation of the needle length. This is illustrated by the needles orthogonal to the viewing direction below in figure 3.12.

Secondly, the counting volume must be corrected. This will directly influence the number density. The counting volume is actually larger than the picture area times thickness, since only a fraction of the precipitate is needed to give one count in the projection. This will give an overestimation of the number density. This effect is illustrated by needles parallel to the viewing direction in figure 3.12.

The derivation of the formulas are not discussed in detail here. The formulas for the corrected needle length $\langle l \rangle$ and number density $\langle \rho \rangle$ are given below by [26]:

$$\langle l \rangle = \frac{\langle l \rangle_m}{1 - \frac{\langle l \rangle_m}{t} \cos\theta \tan\phi} \tag{3.2}$$

and

$$\langle \rho \rangle = \frac{3N}{At(1 + \frac{\langle l \rangle}{t})} \tag{3.3}$$

where

- $\langle l \rangle_m$ is the measured needle length.

- t is the thickness of the sample.

- A is the counting area.

- θ is the angle between the orientation of the[001] and [010] direction relative to the specimen tilt, and is assumed 45° [26].

- $\phi = \arccos[cos\alpha_1 \cos\alpha_2]$ is the angle between the sample normal and the incoming beam. α_1 and α_2 is the is the tilt in the two perpendicular directions in a double tilt specimen holder.
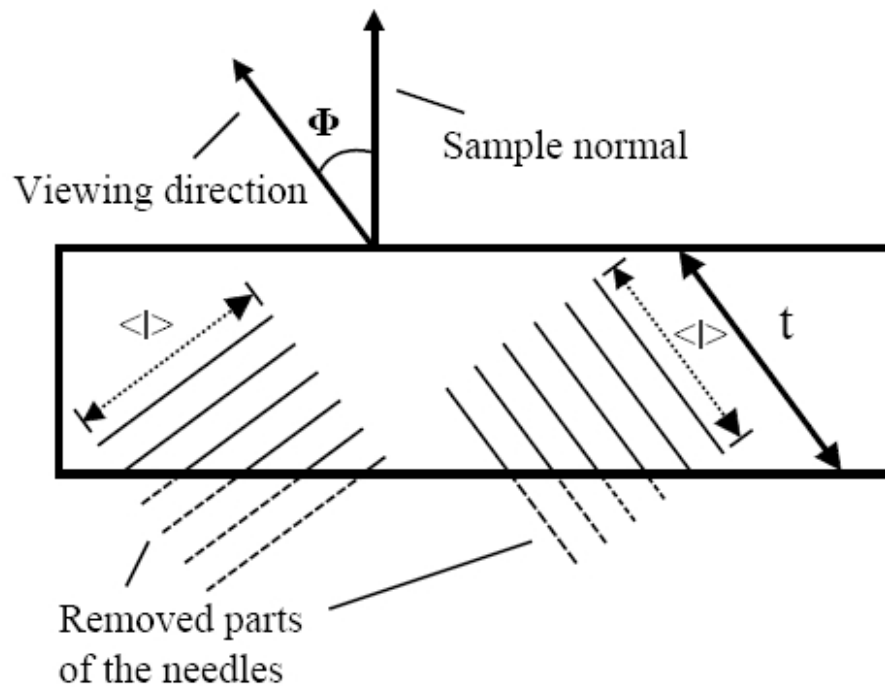
Figure 3.12: The TEM sample with indications of counting errors [8]. Notice that t gives the measured thickness.

Chapter 4

Results

In this chapter the results from the hardness measurements and the microstructure analysis with TEM will be presented. This work is a continuation of the work described in [27], and relevant results are therefore included here. The TEM work is not as comprehensive as the hardness measurements , and this will be discussed under further work in chapter 7. The hardness measurements are complete with 14 different OA times from all of the three heat treatments of the same alloy. Heat treatment one is investigated by TEM.

4.1 Hardness measurements

The hardness is given as the mean of 10 measurements and the error bar in the figures is given by +/- the standard error. The leftmost point is without OA (the curves start at 1 minute since 0 is undefined).

4.1.1 Heat treatment one (HT1)

The hardness curve for overaging at 200°C is given as function of time in figure 4.1 below. This heat treatment gives a maximum hardness just below 80 HV. The hardness fluctuate around 75 HV before a sudden decline at about 600 minutes. The total hardness decrease is about 25 HV. There is observed a double peak in the hardness.
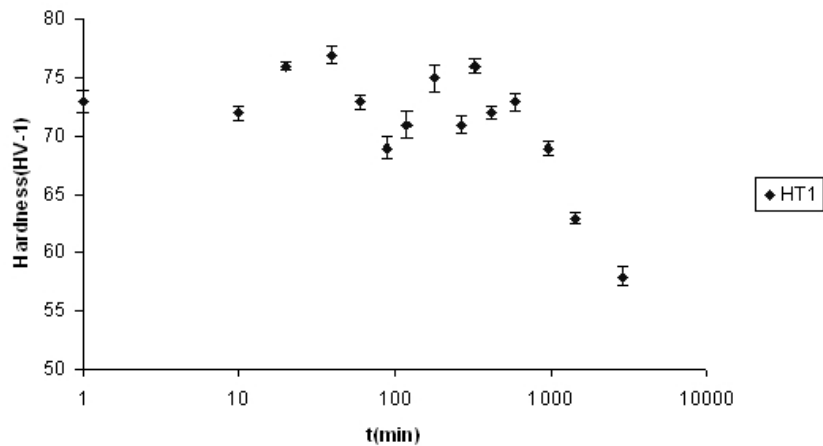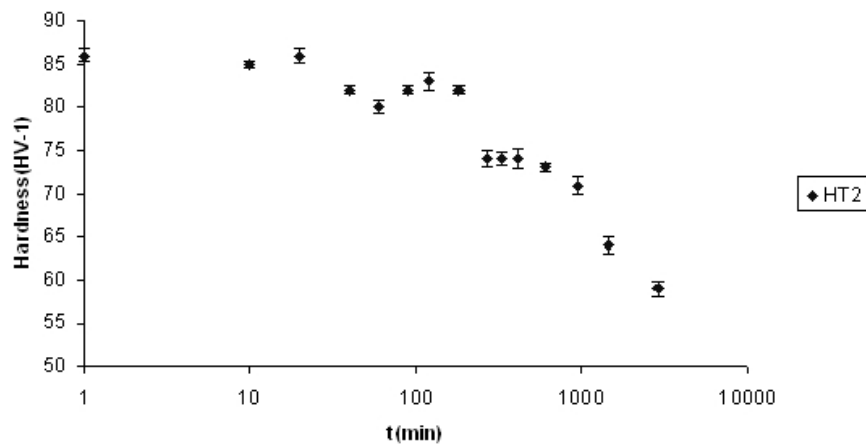
Figure 4.1: Vickers hardness after aging for HT1. This means that the first hardness measurement is for an overaging at 200°C for 0 minutes, the second is point for an overaging for 10 minutes etc.

4.1.2   Heat treatment two (HT2)

The hardness curve for overaging at 200°C is given as function of time in figure 4.2 below. The peak hardness is about 85 HV. This curve also has some fluctuations before the hardness drops off at about the same time as with HT1, about 600 minutes. In this case the total hardness decrease is about 20 HV during the 2880 minutes. There is observed a double peak in the hardness, similar to the one after HT1.

Figure 4.2: Vickers hardness after aging for HT2. This means that the first hardness measurement is for an overaging at 200°C for 0 minutes, the second point is for an overaging for 10 minutes etc.

4.1.3   Heat treatment three (HT3)

A plot of the full hardness curve obtained with HT3 is given below in figure 4.3. After SHT the hardness is very low, at about 40 HV. After the bar has been in the oil bath about 100 minutes, the hardness increases rapidly with about 50 percent. Then there are some fluctuations in hardness before it stabilizes just above 55 HV. As with the two other heat treatments it seems to be a double peak in the hardness, but not as clear as with the previous two double peaks.
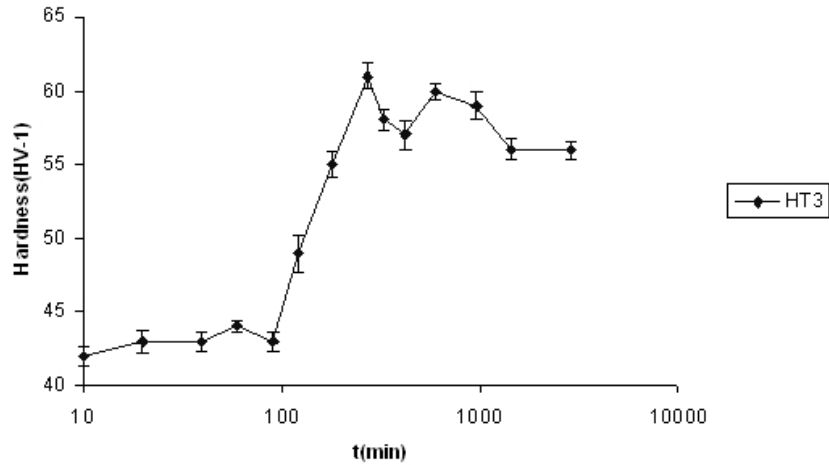
Figure 4.3: Vickers hardness after Solution treatment and during aging followed by overaging.

4.1.4   Comparison of heat treatment one and two

The results given above for HT1 and HT2 are combined here for a comparison. The plot is given in 4.4. They both start to increase hardness at 10 minutes. This is much clearer for HT1 but HT2 seems similar. Then both reach a minimum at about 100 minutes. After this point they seem almost stable before the two curves converge. Then they follow a very similar decrease in hardness.
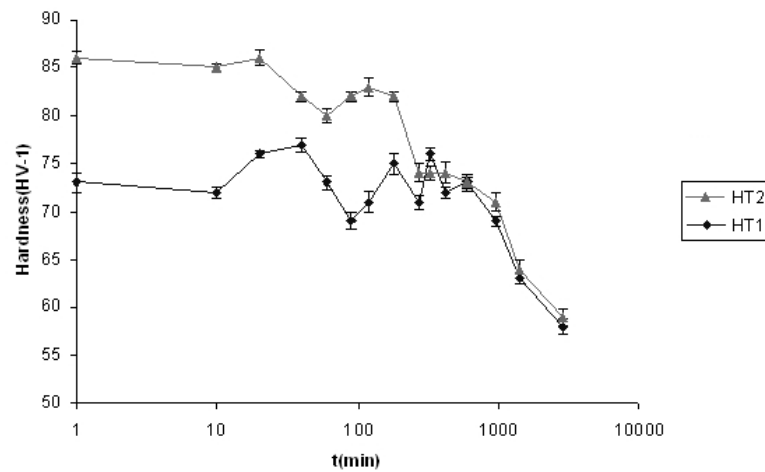
Figure 4.4: Hardness curves for HT1 and HT2.

4.2   TEM results

Based on the hardness measurements, five OA times from HT1 was chosen. Since HT1 was intended to give large precipitates compared to HT2, HT1 was chosen so that the change of precipitates could be easier to observe. The five conditions are shown below in figure 4.5. Points were chosen with OA times evenly spread along the log(t) axis in order to try to get an overview over the transformation process. This assumes that the transformation starts at the beginning of the OA. All pictures were taken by the author, if nothing else is mentioned. All HRTEM pictures were taken by Calin D. Marioara.
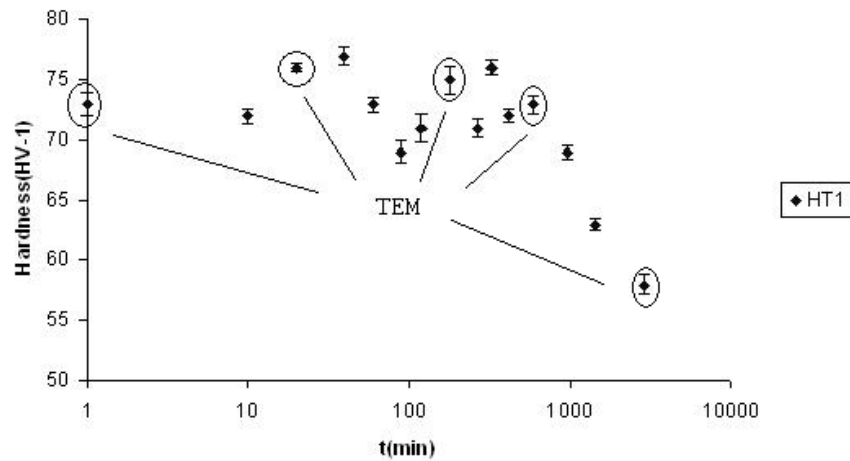
Figure 4.5: The overaging times selected for TEM investigation.

4.2.1   Precipitate microstructure development

The microstructure of the samples overaged at 200°C taken from HT1 at OA times of 0, 20, 180, 600 and 2880 minutes were investigated. First the specimens needle lengths, cross section size and number density was measured. Then the volume fraction was calculated. The measurements and calculations are described in section 3.4.5. Quantitative numbers for the measured quantities are shown below in Table 4.1. TEM images are shown at low resolution (89 kx) in figure 4.6, and at high resolution (492 kx) in figure 4.7. Finally, the results are shown in graphs in figure 4.8.

As seen from the table and figures, the cross section sizes are similar for the first three OA times. After 600 minutes of OA the precipitate cross sections are starting to grow, and they also get a rounder shape, as seen in 4.7 d). The round shape was also found in other images from my project work [27]. The average cross section size is almost doubled after 2880 minutes, and this can be most clearly seen at the low resolution picture in 4.6 e).

The needle length decreases during the first 20 minutes of OA. After this, the needle length increases with longer OA times. There is an especially large jump in needle length from 600 min OA to 2880 min OA. This can be clearly seen in figure 4.6 e).

The number density has a very large increase during the first 20 minutes of OA. This can be clearly seen in figure 4.6 a) and b). Then the number density decreases with longer OA times. After 600 minutes the number density is almost the same as it was when overaging was started. This can be observed by comparing figure 4.6 a) and d). After 2880 minutes the number density has decreased drastically, as seen in 4.6 e). Notice that the behavior of the number density is opposite of the needle length(U-shape and inverse U-shape) . The change in number density is much larger than the change in needle length early in the OA. This can be seen in figure 4.8. The shape of the number density curve is similar to the hardness curve for HT1

given in figure 4.1. But there is no double peak in the number density curve. Also, the change in number density is much larger than the change in hardness.

The volume fraction is proportional to the other above quantities. Therefore it follows a similar behavior to the number density up to 600 minutes, because the length and cross section size does not change as much as the number density. This is seen in figure 4.8 c) and d). After 2880 min there seems to be an increase in volume fraction compared to 600 minutes OA.

The precipitates nucleate homogenously in the material, with some exceptions, as illustrated by e.g the heterogenous nucleation on the dislocation in figure 4.6 a).

Table 4.1: Microstructure parameters for HT1 during overaging. The table shows cross section, needle length, number density and volume fraction. It also includes the standard error.

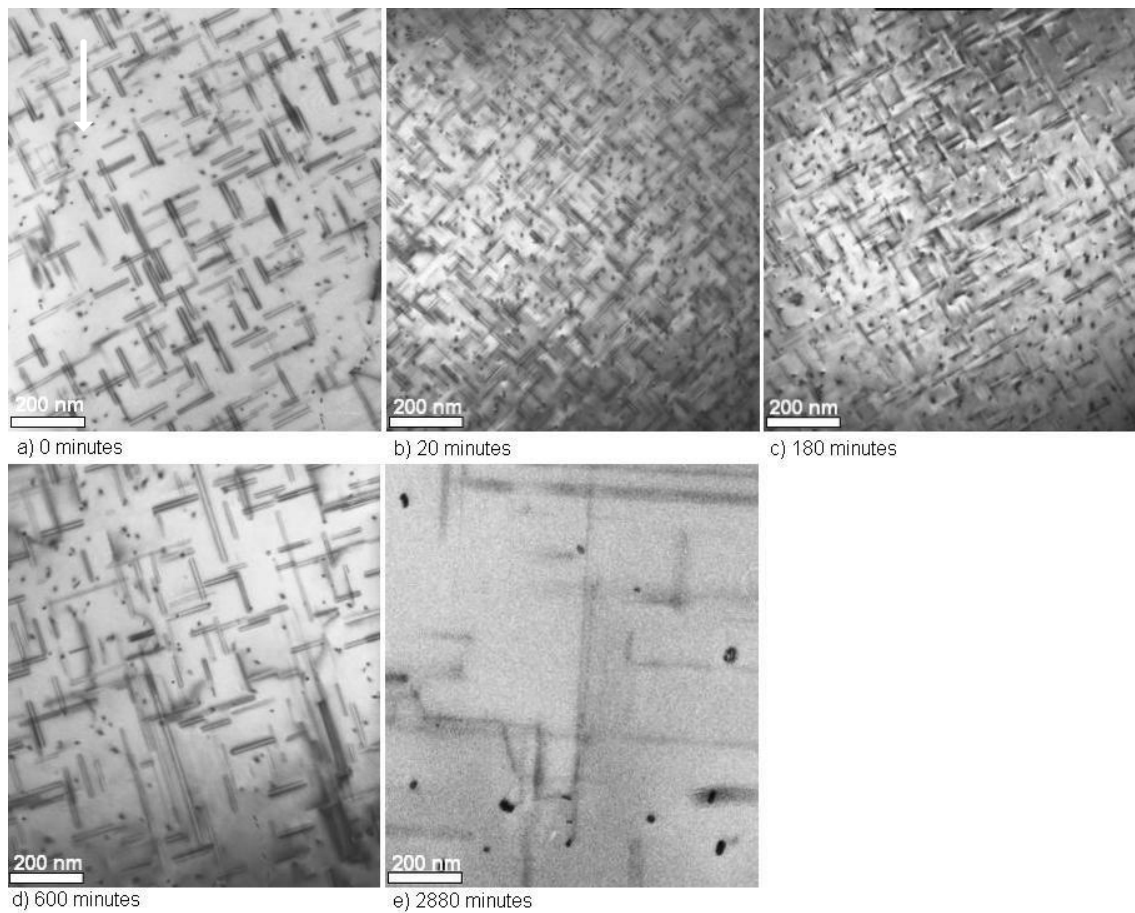| Overaging time (min)	Cross section nm^2	Needle length (nm)	Number density (μm^{-3})	Volume fraction (10^{-2})
0	28.56±1.06	94.34±1.95	2490± 268	0.67±0.08
20	32.54±2.46	56.31±1.30	7280± 753	1.33±0.17
180	29.60±1.60	72.05±2.10	5800± 616	1.24±0.15
600	37.20±1.71	79.36±3.97	2210± 239	0.65±0.08
2880	58.42±6.69	425.3±17.3	319± 41	0.79±0.14

Figure 4.6: a)- e) shows the microstructure for the different OA times. The magnification is 89 kx. The thicknesses for pictures a) - e) were 171 nm, 173 nm, 138 nm, 149 nm and 169 nm, respectively. Since all pictures have similar thicknesses they can be directly compared in order to observe the number density change. The arrow in a) shows nucleation on a dislocation. Picture a) was taken by Calin D. Marioara.
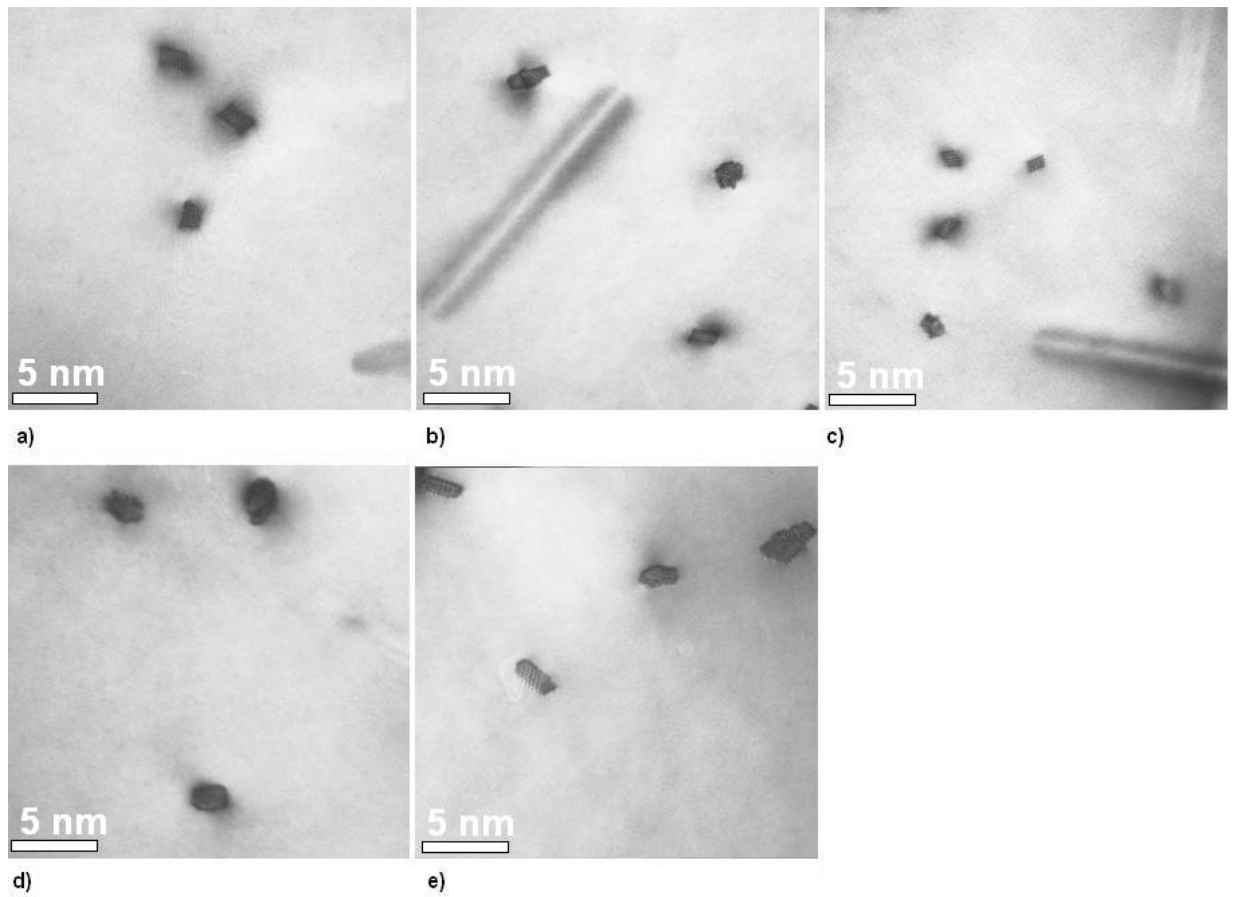
Figure 4.7: a)- e) shows the microstructure for the different OA times of 0, 20, 180, 600 and 2880 minutes, respectively. The pictures were taken at a magnification of 492 kx . Pictures a) and b) were taken by Calin D. Marioara.
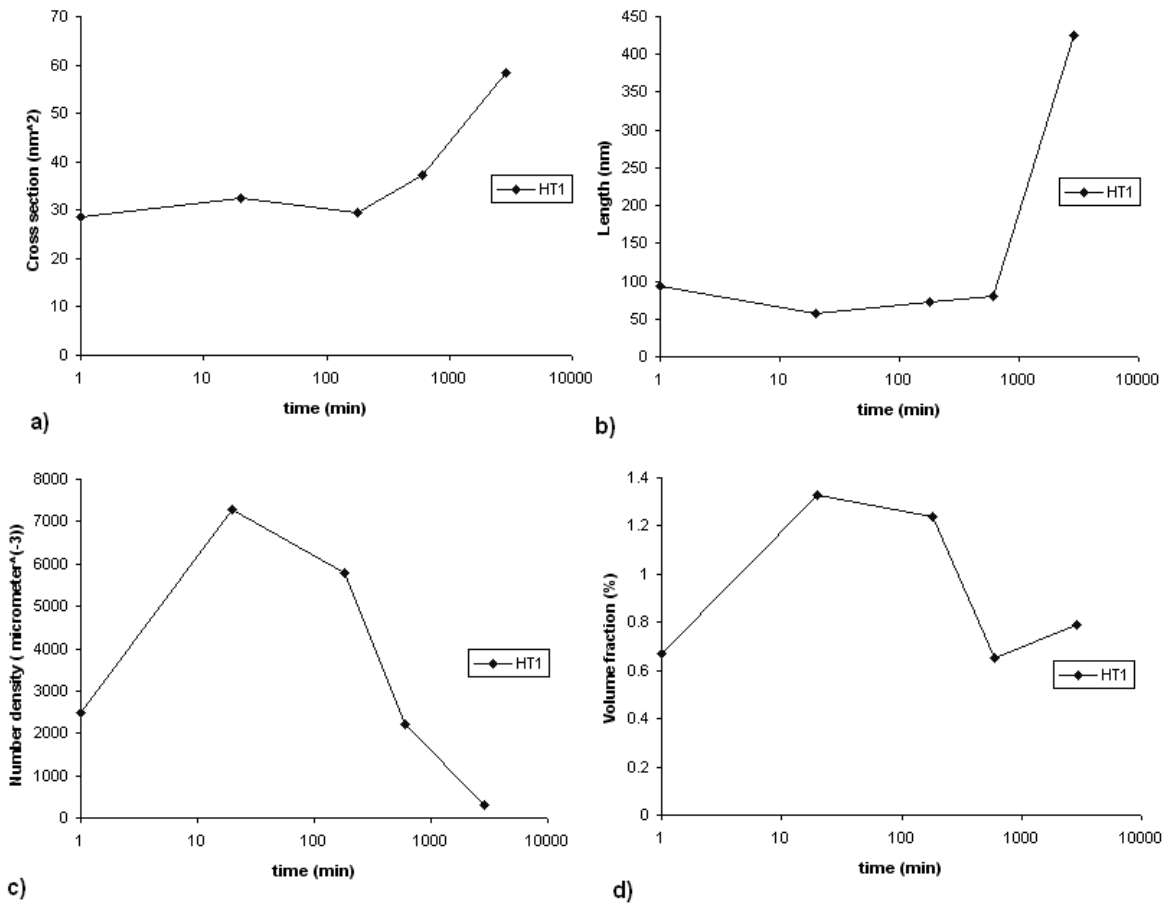
Figure 4.8: Statistics for overaging with heat treatment HT1. a) shows the cross section. b) shows length. c) gives the number density and d) shows the volume fraction. The errors are given in table 4.1.

Amount of β'' precipitates

In addition to measuring the above quantities, each precipitate were investigated to find out if it was overaged or not. First all β'' **precipitate cross sections** were counted, then the **total number of cross sections** were counted. This was done for each picture. They were labeled β'' if the characteristic rhombohedral shape was seen or the unit cell of β'' was identified. An example of an identification can be seen below in figure 4.9. The fraction of β'' was obtained for each OA time by summing up the total number of β'' and the total number of cross sections from all the pictures included. This will give an indication of how many particles that have been transformed or overaged. A more detailed investigation of precipitates will be given with the results from the HRTEM section below.
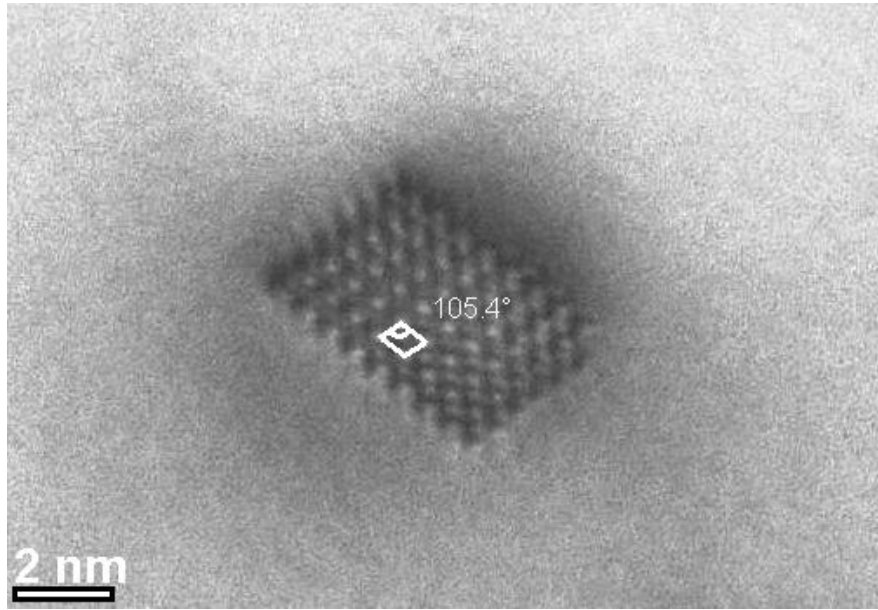
Figure 4.9: Identification of a β'' particle with an image from the CM30. The measured angle was about 105°, and the true angle is written in the figure as a reference.

The images that were used were of good quality, and all precipitates from each picture was counted. At least 30 precipitate cross sections were used from each condition. For the OA time of 600 minutes 12 cross sections from the HRTEM images were included in the statistics, since only 4 images could be used from the CM30. Examples of some of the images included from the CM30 are given above in figure 4.7. The results are shown below in table 4.2. The fraction of β'' is plotted in figure 4.10.

The fraction of β'' is almost constant the first 180 minutes of OA. After 600 minutes the fraction starts to drop off, and after 2880 minutes there is almost no β'' precipitates. Notice that the behavior of the fraction of β'' is similar to the behavior of the cross section size and needle length given above in 4.1. During the first 180 minutes the change is rather small. Then a large change occur in the last two time steps. The fraction is inversely correlated to needle length and cross section size since it decrease while the other two increases.

Table 4.2: Fraction of β'' during OA. The

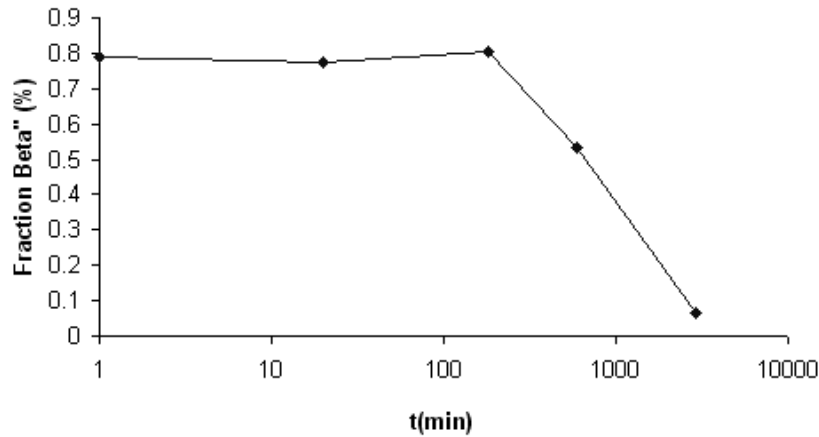| Overaging time	number of β''	total	% β''
0	26	33	79
20	45	58	78
180	37	46	80
600	16	30	53
2880	2	30	7

Figure 4.10: The fraction of β'' during overaging.

4.3 High Resolution TEM

For a more in-depth characterization of the microstructure, HRTEM was performed in order to determine the type of precipitates during the heat treatment. Based on the above results, especially that most of the change in microstructure occurs during the two last time steps in the overaging, led to the investigation of the two last OA times from the HT1 heat treatment. This means that the samples investigated here was aged as described in HT1, and then overaged for 600 and 2880 minutes at 200°C. Representative precipitates from both OA conditions are found below in figures 4.11 to 4.17. The different precipitate types are shown in table 4.3.

4.3.1 Precipitates containing the β'' phase

Many of the precipitates investigated by HRTEM turned out to have some other phase growing on the boundary of a perfect β'' phase. Such growth is called heterogenous nucleation. Most of the phases growing were disordered, as seen below in figure 4.11 and 4.12. In some of the images the growth was large enough to identify the phases, either by observing the unit cells in real space or by looking at the fast fourier transform (FFT). If a hexagonal pattern was found in the FFT, it was concluded that the phase was post -β''. An example is shown in figure 4.13. The orientation of the β'' unit cell with respect to the Al matrix could also be checked, since the angles are known, and the matrix is visible.

The six first images in figures 4.11 and 4.12 are from an OA time of 600 minutes, while the two last ones shown in figure 4.12 c) and d) are taken from an OA of 2880 minutes. The first six images shows precipitates with small and intermediate sized growths. The last type of particle with large growth on both sides was only found in the sample overaged for 2880 minutes. These precipitates were also the only ones in the 2880 minutes sample that showed any sign of the "old" perfect rhombohedral β'' shape seen in samples that were less overaged. Figure 4.14 shows another β'' precipitate with growth on both sides. In figure 4.12 c) and d) the growth

is identified as U2, while the growth in figure 4.14 is identified as β'. A table showing the different precipitate types is given below.
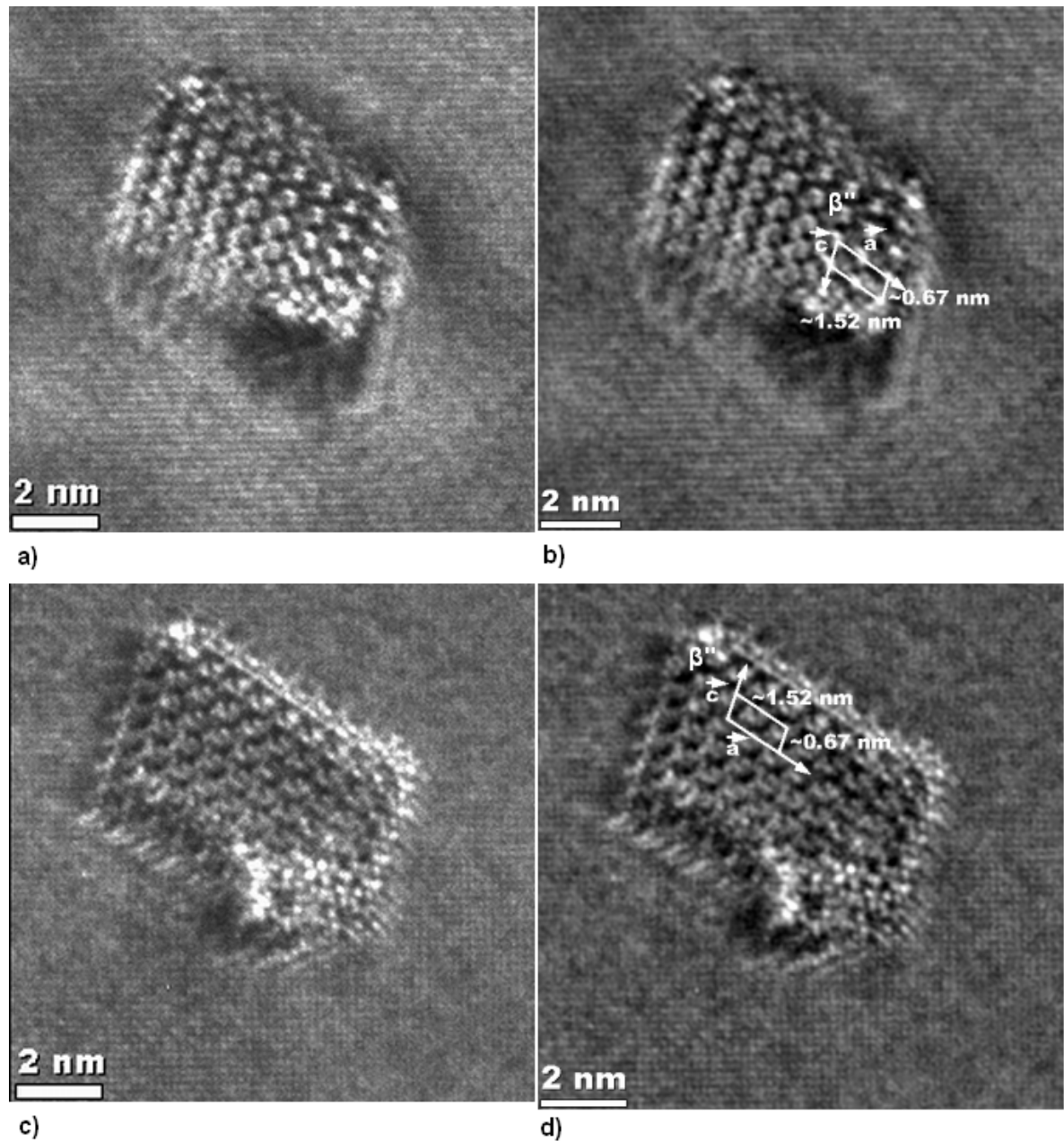

Figure 4.11: HRTEM images from the HT1 heat treatment overaged for 600 minutes at 200°C. a) shows the raw image of a perfect β'' particle. b) In order to reduce noise , a Fourier filter was applied as described in the experimental section. One β'' unit cell is shown with lines and unit vectors. c) shows the raw image of a β'' particle with a small growth on the lower side. d) Fourier filtered image of c). The β'' part is identified and a unit cell is shown with lines and unit vectors. The small growth is not identified.
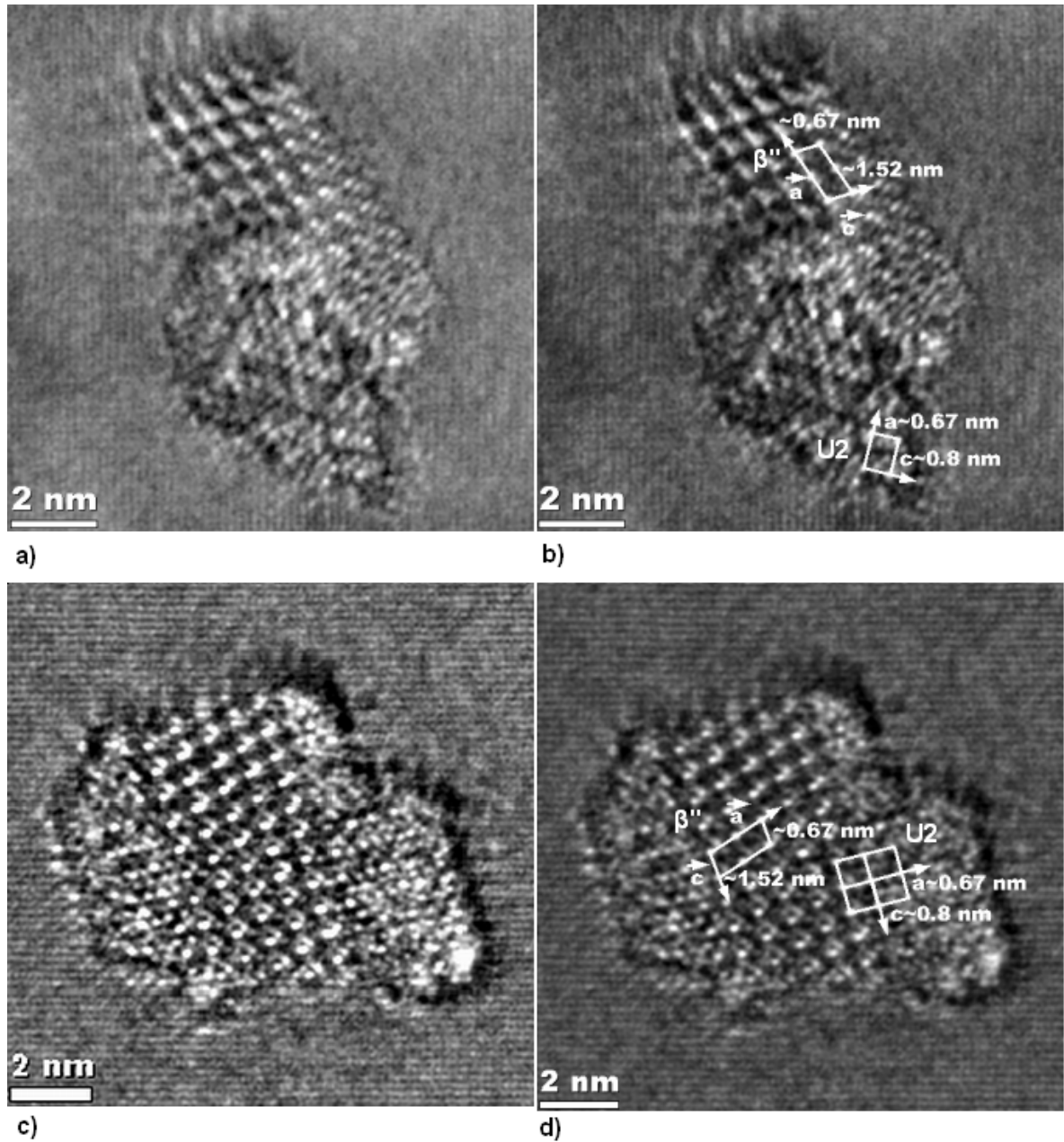
Figure 4.12: HRTEM images from the HT1 heat treatment overaged for 600 minutes (a and b) and 2880 minutes (c and d) at 200°C. a) shows the raw image of a β'' particle with a large growth containing a U2 unit cell. b) In order to reduce noise , a Fourier filter was applied as described in the experimental section. One β'' unit cell is shown with lines and unit vectors. The U2 unit cell is also indicated. c) shows the raw image of a β'' particle with growth on both sides. Notice that the perfect shape of a β'' particle can be observed. d) Fourier filtered image of c). The β'' part is identified and a unit cell is shown with lines. On one side the growth as identified as U2 with several unit cells indicated with lines.
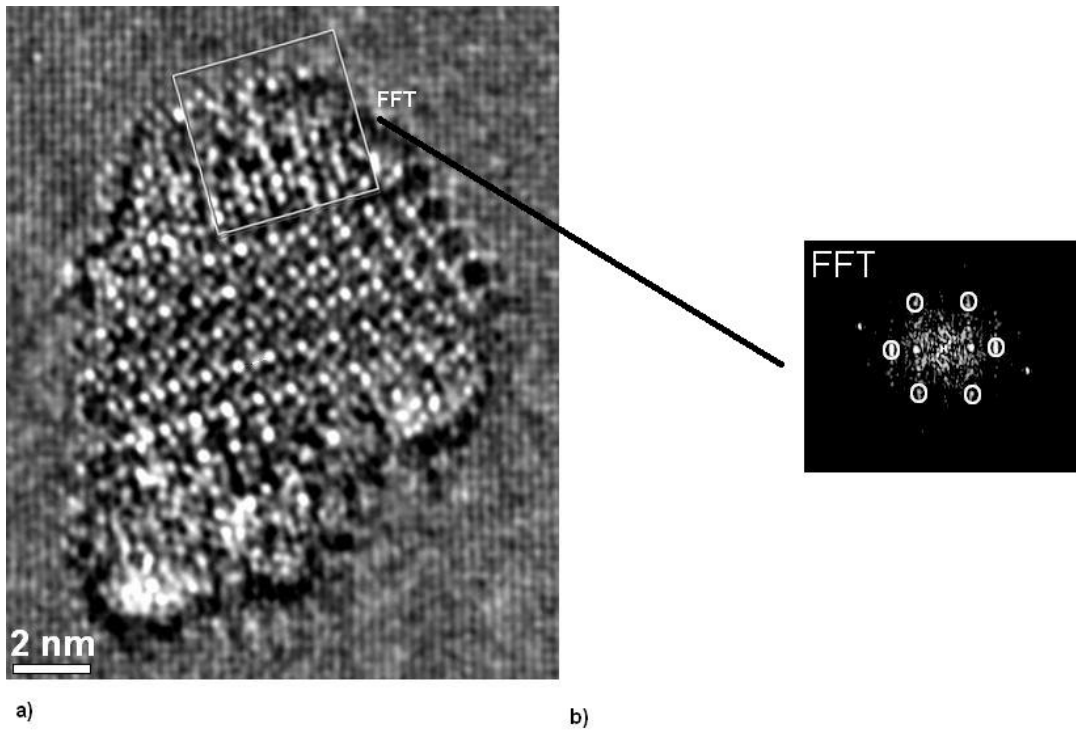
Figure 4.13: a) Further investigation of the particle in figure 4.12 c) where a selected area is indicated. b) FFT of the area indicated in a). Notice the hexagonal pattern indicated by rings. This suggest that the indicated area is post- β''.
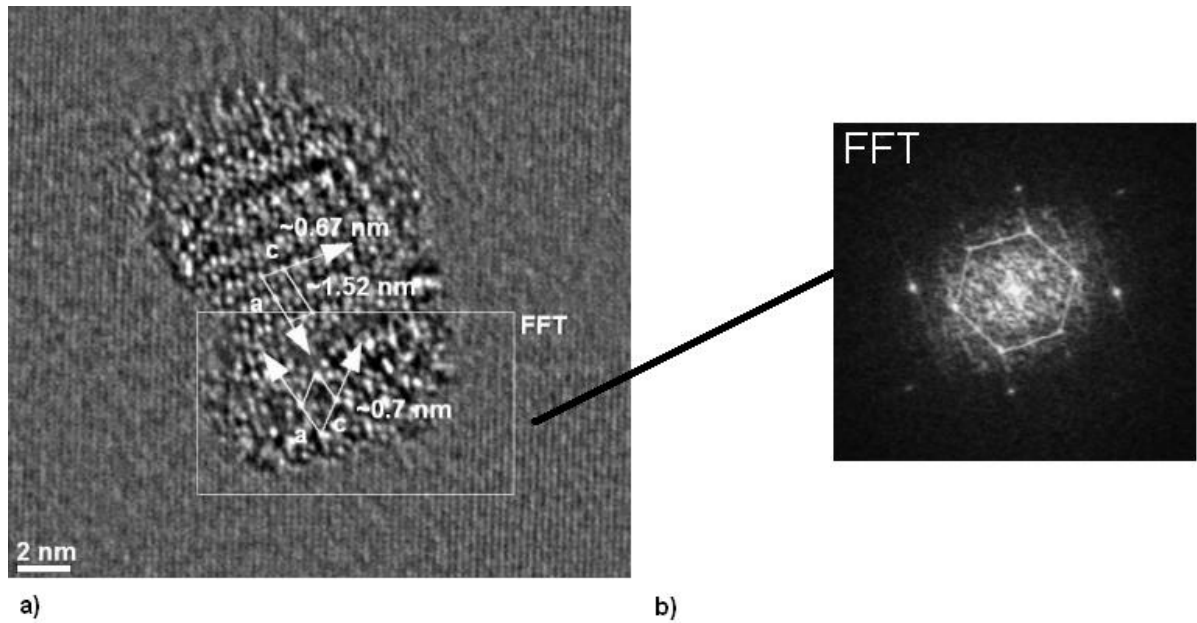
Figure 4.14: HRTEM images from the HT1 heat treatment overaged for 2880 minutes at 200°C. a) shows a filtered image of a β'' particle with a growth with a β' unit cell. b) FFT of the selected area in a) showing that the growth has a hexagonal pattern in the FFT.

Many of the β'' cross sections with a rhombohedral shape are elongated in one direction. The elongation is observed both along the a and c unit cell vectors, but any statistics of which is more common is not made. In most of the images the growth is along the elongated side of the precipitate cross section. But this is not always the case, and below in figure 4.15 a growth can be observed on the short side of the precipitate cross section.
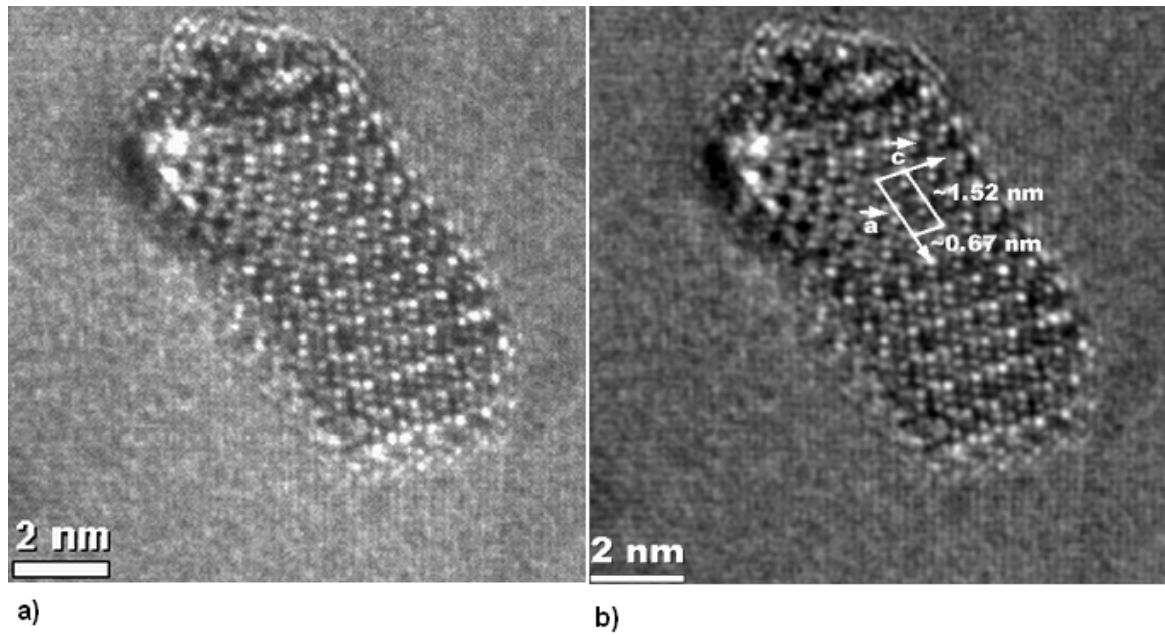
Figure 4.15: HRTEM images from the HT1 heat treatment overaged for 600 minutes at 200°C. a) shows the raw image of a β'' particle cross section with a small growth on the boundary of the short side of the precipitate. b) Fourier filtered image of a) where a β'' unit cell is drawn with lines and vectors.

4.3.2   Precipitates containing post- β'' phases

The majority of the post- β'' precipitates investigated where found to contain various degree of disorder. This can be seen below in figure 4.17 a) where the rightmost part of the particle does not have a clear rectangular periodicity expected in the U2 phase. All post- β'' phases where found in the sample with a OA time of 600 minutes, and all except B' was found in the sample with a OA time of 2880 minutes. The amount of overaged phases can be found below in table 4.3.
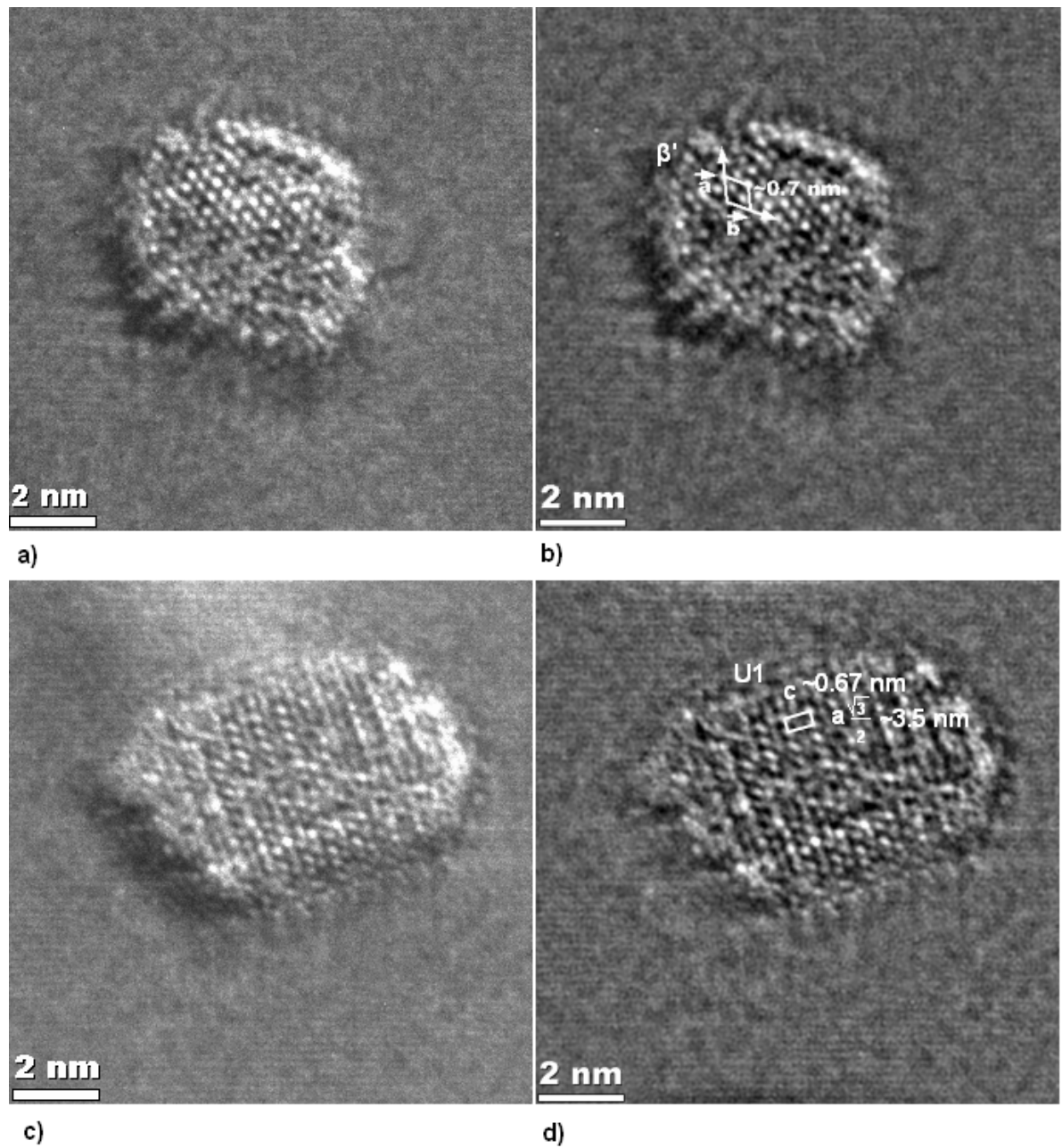
Figure 4.16: HRTEM images from the HT1 heat treatment overaged for 600 minutes at 200°C. a) Raw image of a precipitate cross section showing the β' phase. b) Fourier filtered image of a) where a β' unit cell is indicated. c) Raw image of a precipitate cross section showing the U1 phase. d) Fourier filtered image of c) where a projection of the unit cell is shown. Since the material is viewed in the $[100]_{Al}$ direction the shortest distance observed is $a\frac{\sqrt{3}}{2}$ [19], where a is the length of the a unit vector in the U1 phase.

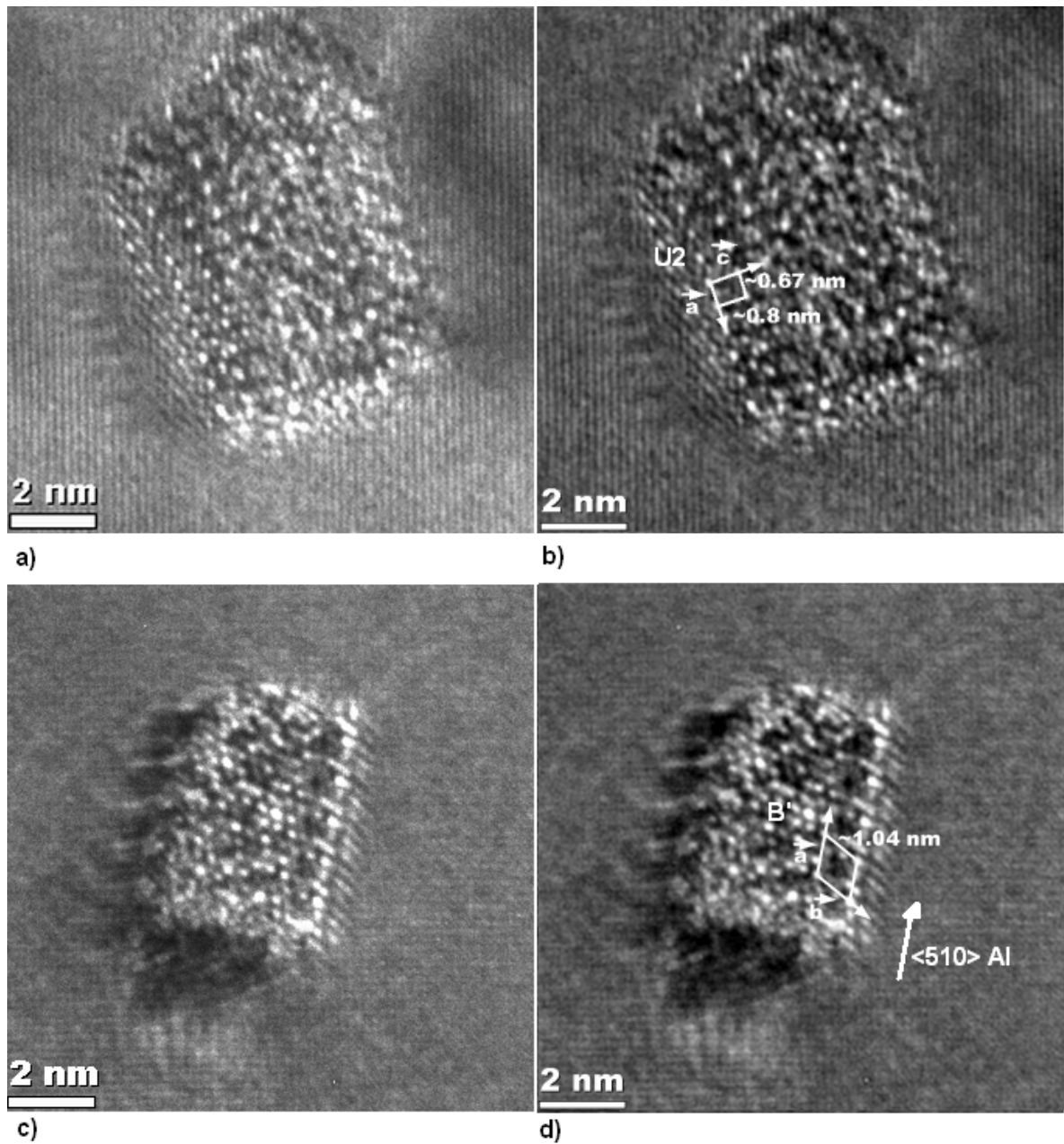Figure 4.17: HRTEM images from the HT1 heat treatment overaged for 2880 minutes (a and b)and 600 minutes (c and d) at 200°C. a) shows a raw image of a precipitate cross section with the U2 phase. b) Fourier filtered image of a) where the U2 unit cell i indicated. c) Raw image of a B' particle. d) Fourier filtered image of c) where a B' unit cell is indicated. The $< 510 >_{Al}$ direction is also indicated. This is parallel to one of the B' unit vectors.

4.3.3   Precipitate types

Again the precipitate types are investigated, but this overview has two major differences from the table shown in section 4.2.1 made from images with lower resolution. Firstly this investigation has identified more types of precipitates, not only the β''.

Secondly it covers only two of the five samples included in the TEM study.

The precipitates were grouped into four types. The first was perfect β'' type. Motivated by the findings in the HRTEM figures that showed β'' particles with growth, the second type was called $\boldsymbol{\beta''}$+ **growth**. Many of the post- β'' precipitates were identified by the hexagonal pattern in the FTT. Such identification does not give knowledge about which of the overaged phases that are identified. Therefore, these results were combined with the post- β'' precipitates that were identified in real space to form the type **post- $\boldsymbol{\beta''}$**. The remaining precipitates that was identified neither in real space or in a FFT, was labeled **unknown**. The results are shown below in table 4.3 and visualized in figure 4.18.

In figure 4.18 it can be seen that the fraction of post- β'' increases with OA time. The fraction of β'' is similar to the one found by the pictures with lower resolution in section 4.2.1. This means that the fraction decreases from about 50% to zero during the last OA step. The fraction of β'' + growth is similar for both OA times, but as mentioned the growths found after 2880 minutes were larger.

Table 4.3: Number of precipitates of each type from HRTEM.

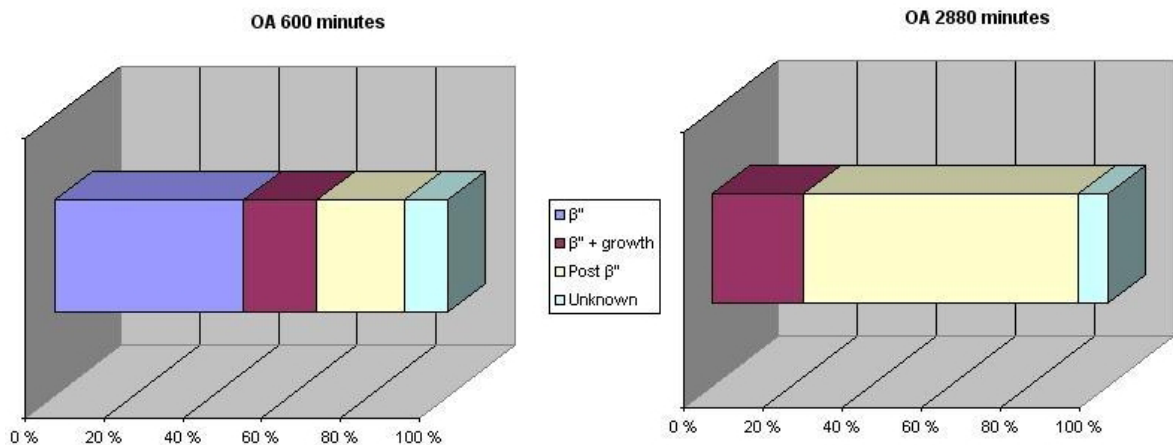| Overaging time	600 min	2880 min
β''	13	0
β'' + growth	5	3
Post- β''	6	9
Unknown	3	1
Total	27	13

Figure 4.18: Graph over the precipitate types given in the table 4.3.

Chapter 5

Discussion

5.1 Hardness measurements

HT1 is discussed first since this was examined by TEM. The hardness curve given in figure 4.1 shows that there is a local minimum. When the hardness finally drops down it does so by an almost linear manner in the log(t) diagram. For a different industrial alloy (6082) treated to peak hardness with a similar Si/Mg ratio, the hardness curve shows an almost linear decrease in log(t), and in addition there is a local minimum [11]. The main difference is the hardness values and at which time each element occur. The minima and linear slope are at very different times, but that could be explained by differences in the heat treatment. The alloy in [11] is treated for longer times at higher temperatures before OA. So the present results seem to be in agreement with these results.

The curve for HT2 has a higher hardness when OA begins. This can be explained by the expected microstructure. Based on previous experiments, HT1 should give a few large β'', whereas HT2 should give many small. The effect of this is explained in section 2.2.2, where it says that semicoherent particles (like β'') will create strain fields that obstruct movement of dislocations. Movement of dislocations typically occur during plastic deformation. A high density of these particles would thus give a greater hardening effect, since the movement of dislocations becomes increasingly harder. The shape of the curve is similar to the one from HT1, and thus have the same similarities shared with the work done in [11]. The similarities of the hardness curves for HT1 and HT2 shown in 4.4 supports that there is indeed some change in the material in the fluctuating region, and not just random noise due to inaccurate measurements. The minima in 4.4 occur both after about 100 minutes, and the sudden decrease in hardness start at 600 minutes for both heat treatments.

Finally, the hardness curve for HT3 is given in figure 4.3. The hardness is much lower at the starting condition compared to HT1 and HT2. This can be explained by the fact that the measurements starts right after SSSS, and the aging is omitted. In section 2.5.3 it says that aging gives the maximum hardness, so when this is not performed the starting point is much lower. But while in the oil bath the hardness increases to a maximum at 270 minutes. So for this heat treatment that would correspond to the aging time in order to reach peak hardness. So if 270 minutes

corresponds to maximum hardness, the minimum at about 100 minutes from the two previous treatments could be expected to occur at about 370 min. There is observed a minimum at 420 min, but since there are no points between 330 and 420 min the minima could in fact lie in between, and thus the same behavior is observed once again. But since the heat treatment is very different from HT1 and HT2, exactly the same behavior is not expected. The sudden drop off observed in HT1 and HT2 does not occur. But since this treatment gives a much lower hardness, it do not have to change the microstructure that much before reaching a more stable configuration. The final hardness lies between 55-60 HV for all treatments, and suggests that the final microstructure when treated for a long time at 200°C is independent of the heat treatment. This is in agreement with [11], where one treatment does OA from T6 (similar to HT1 and HT2), and the other is similar to HT3, but with storing at room temperature after SSSS.

5.2   TEM

Just by looking at the hardness curve for HT1 given in figure 4.1 indicates that the overaging is slow, since the first large drop in hardness comes after 1440 minutes of OA. But it was not easy to conclude that the transformation of β'' does not start before this point based only on the hardness curve. Therefore samples that where chosen to be investigated by TEM were evenly spread over the OA times. But when the statistics were obtained, as shown in figure 4.8 and 4.9, it confirmed that there was little change in the precipitate structure before 180 minutes of OA. Therefore the HRTEM pictures were chosen from the two last conditions since they were considered most interesting for observing the change from β'' to post- β'' phases. But if this information was known in beforehand, more samples towards the end of the hardness curve would have been chosen to investigated by TEM to get a clearer and more detailed description of what happens during the large drop in hardness.

5.2.1   Precipitate microstructure development

The final microstructure after 2880 minutes of overaging shows similar number density, length and cross section size as the 6082 alloy [11] mentioned above in the discussion of the hardness curves. The alloy is heat treated after peak hardness for 3 hours at 260°C, and is called H2/A3/3h. In the present work the alloy is treated for a longer time at a lower temperature, but it seems that the total effect is similar on length, cross section size and number density.

The image in 4.6 d) show that the particles loose their sharp edges. This is related to the nucleation theory discussed in section 2.6.1. At a given time, the system will minimize the total energy by changing the surface and the bulk of the precipitates. Precipitates nucleating far out in the OA are less coherent with the matrix, creating a higher interfacial energy [10]. This increase in surface energy is compensated by a decrease in bulk energy, since the phase is closer to equilibrium [10]. Allowing for higher interfacial energy could explain a change in observed cross section. But since none of the energy terms can be determined here, this will not

be discussed further. The change of the interface shape was mainly observed in the images with lower resolution taken from the CM30, and it may also be due to small growths that the interface appear different in these images. But in either case something is happening on the precipitate/matrix interface.

Since a high number density obstruct dislocation movement and makes the material harder, a correlation between these two parameters are expected. The number density has a similar form to the hardness curve for HT1, but the double peak is not observed. But since the number of data points are much smaller for the number density measurements, a double peak in number density could exist even tough it is not observed in these measurements.

The fact that the volume fraction is higher than the solute fraction can be due to aluminium in the β'' precipitates. The solute fraction of 1.04 wt% is almost within the error for the highest volume fraction of 1.33-0.17 = 1.15 wt%. The remaining error can be due to non-uniform distribution of the precipitates in the specimen, and other measurement errors on in the statistics. The measurement errors are discussed later. In the work done in [11] multiple alloys investigated showed a higher maximum volume fraction than the solute fraction. The conclusion from these results should be that most of the solute is in precipitates at such high volume fractions, but whether it is below or above the solute fraction is not clear.

After 20 minutes of OA the number density gets a large jump by a factor of three . Then, during the next 480 minutes the number density drops down to the same level as it started with at OA of 0 minutes. This could suggest that the time it takes to nucleate is much shorter than the times it takes to dissolve the precipitates. Since no change occurs in the precipitate type during the first 180 minutes of OA, the event of rising volume fraction and number density is therefore considered to be unrelated to the transformation of β''. But the drop in volume fraction from 180 minutes OA to 600 minutes of OA is just as large as the increase in volume fraction from 0 to 20 minutes of OA (a factor 2). Due to the fact that this drop coincides with both the emergence of growths on the β'' seen in the HRTEM images and the "rounding" of the sharp edges, it is more probable that this drop in volume fraction are related to a transformation of β''. If growths emerge on the β'' particles, solute has to be available in the Al matrix, and this can explain the large drop in volume fraction before the growths emerge. These growths will be discussed further in the next section.

5.2.2   Transformation of β''

The fact that perfect β'' particles and post- β'' particles coexist in the sample overaged for 600 minutes suggests that there are local variations in the material influencing the time scale for the overaging of each precipitate. In this work only two samples were investigated by HRTEM, but if each sample represent a time interval rather than one point in time, multiple "time steps" of a transformation could be obtained from one sample. The images from figures 4.11 to 4.12 showing β'' particles with small and intermediate sized growths after 600 minutes OA and large growths after 2880 minutes OA, could be used to make a model for the transformation of

β''.

   This is a simple model only describing the precipitate cross sections and will be presented by a figure. The strain at the precipitate/Al- matrix interface and other interphases are not indicated in the figure, but they will be discussed later. The shape on the post- β'' phase cross section was randomly chosen and does not indicate anything about the real phases. The model is given below in figure 5.1.
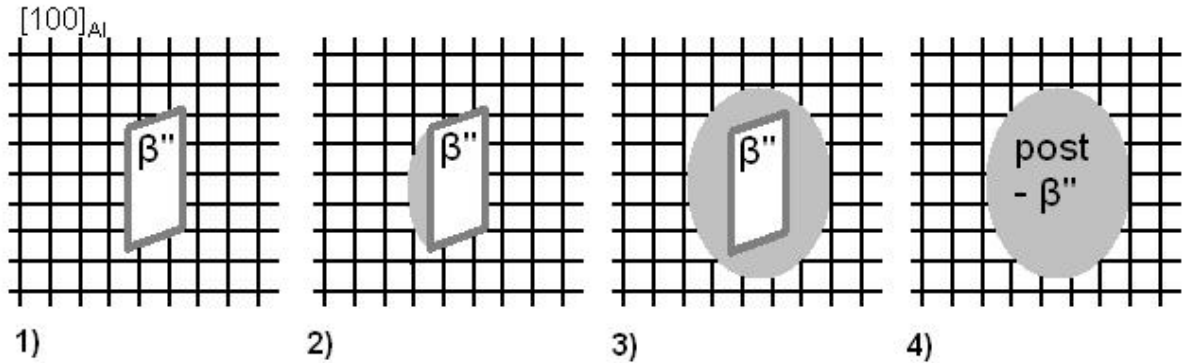

Figure 5.1: Proposed model for the transformation of β''. The black lines indicate the Al matrix. 1) shows a perfect β'' particle cross section. 2) shows the same particle with a small growth representing the early stages of post- β''. 3) has a β'' particle completely surrounded by a post- β'' phase. 4) A post- β'' particle in the Al matrix.

   The steps 1)- 3) in figure 5.1 can be directly deduced by observing the HRTEM images, β'' particles with different growths are observed. Step 3) is not actually directly observed, but by considering figure 4.12 d) and 4.15 it was seen that growths can occur on both the short and elongated interfaces of the precipitate, it should be only a matter of time before the post- β'' phase surrounds the β''. In a work describing the U2 phase [28] it is noted the $\mathbf{c}_{\beta''}$ and $\mathbf{a}_{U2}$ vectors are common, and that there are close structural relations between the phases. With a closer look at 4.12 d) it is seen the growth is in fact normal to the $\mathbf{c}_{\beta''}$ and $\mathbf{a}_{U2}$ vectors. The figure is repeated here with some new lines indicating the growth and the direction. So the findings of the growths are in agreement with work the work done in [28].
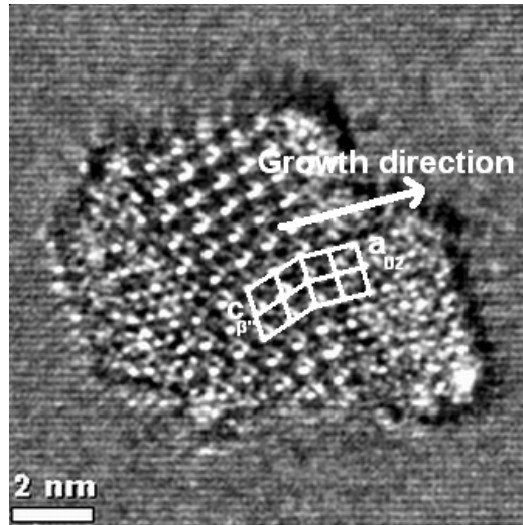
Figure 5.2: The growth direction for the growth on a β'' particle. The $c_{\beta''}$ and a_{U2} sides are indicated.

The suggestion of 4) as the final step in the transformation is made because particles with large growths similar to the one in figure 5.2 are seen at such a late stage in the overaging. Also, no other signs of further transformation before the final post- β'' are observed. Therefore it is assumed that the next step for these particles surrounded by post- β'' phase will be to rearrange the atoms of the β'' phase into post- β'' phase. This means that the last step in the model will be an internal transformation. It was mentioned above in section 4.3.2 that most of the post- β'' phases were disordered. Such disorder has also been observed before in [28]. This can indicate that there are internal transformations in the post- β'' phases, supporting the last step in the model. Internal transformation of the β'' to post- β'' has been proposed before in Huis et al. [29], and will be referred to as an direct transformation. But the new information found above that is indicated by step 3) in the model has one important difference compared to a direct internal transformation from β'' to post β''. The β'' is surrounded by post- β'' before the transformation. In the case of a direct transformation, the matrix/β'' interface will change to a matrix/(post- β'') interface. In the case of the internal transformation in the model, the interface will change from β''/(post- β'') to (post- β'')/(post- β''), i.e the interface will disappear. Since every interface has an interface energy, the internal transformation in the model will require less energy. These energy considerations supports the internal transformation in the model.

Due to the large drop in number density and volume fraction, another mechanism for transformation could also be that post- β'' particles nucleated in the matrix because of the high availability of solute. Then it could be expected that a group of small post- β'' particles would emerge. The distribution of cross section size and needle lengths were inspected to check if there was e.g one group of small particles and one group of much bigger. This could indicate that one type of particles were dissolved when another was growing. This would lead to a double peak in the size distribution, but no such peaks were found. But some small post- β'' particles where observed, so nucleation in the matrix could be an alternative transformation

mechanism.

The results from [11] show that the Si/Mg ratio is important for which phases that nucleate. It was found that with a similar Si/Mg ratio as in this work, most of the post- β'' were of U2 type. So the transformation process described in the model can be limited to only one or a few of the four known post -β'' phases. One of the biggest weaknesses of the model is that it cannot be concluded from the statistical data that this is the main mechanism for transformation of all β''. An even higher occurrence of the precipitates with growth would strengthen that the model was correct. If there were investigated more samples between the two selected for HRTEM studies, a better overview and more statistical data could have been obtained. There could be some missing links in the model due to the low number of samples investigated. The model is based on the assumption that the different sizes of the growths are due to different transformation times locally, since different "time steps" were from one sample. It would have been better if more of the different particles actually were from different overaging times, so that the time evolution would have been clearer. In this work only the largest growths were exclusive to the last sample, while the others were found one time step before.

5.3   Error discussion

5.3.1   Hardness measurements

In the figures presenting the hardness measurements, there can also be seen errors bars. These bars are a result of that each condition had 10 measurements. The differences from each of the measurements results from reading errors, roughness of the sample, non horizontal surface and other unsystematic errors. Systematic errors can come from e.g. bad calibration of the hardness machine and work hardening of the sample during cutting etc. In order to eliminate work hardening of the sample it should be ground. In the present work all the measurements for each OA time was done on different cylinders. In order to reduce the error all measurements could have been done on the same cylinder. Considering these error sources the hardness measurements should be expected to show a general trend, but small fluctuations as shown just before t = 600 in figure 4.5 should be disregarded.

5.3.2   TEM work

The pictures were taken in a systematic manner in order to avoid duplicates, and also inspected after to look for mistakes. Scale bars were found using a script in a program called Digital Micrograph. These seem reasonable when comparing with the known distances in the pictures, e.g the size of the β'' unit cell.

The counting procedure in section 4.2.1 is dependant on the subjective opinion of the author of which particles are perfect β'' etc. This decrease the validity.

The needle length was hard to measure since it relied on the contrast of the strain field. Sometimes it was very hard to see where a needle started and ended. This could lead to a considerable error. Especially for the sample with an OA time

of 2880 minutes the needle length was hard to measure. The cross sections where clearer than the needles, and the error due to measurements should be smaller. The uncertainty of the thickness error can be estimated to about 10%.

The HRTEM pictures contained only one precipitate per picture, and since the TEM operator chooses all the precipitates, this can lead to poor statistics. In this work the operator of the HRTEM was not the author, which hopefully led to a more random selection of precipitates. A higher use of FFT for the identification of particles found with HRTEM could confirm that the precipitates were of the type found in real space. But many of the FFTs where hard to use due to the disorder in many of the post- β'' particles.

Chapter 6

Conclusions

Phase transformation during overaging has been studied in an Al-Mg-Si alloy through TEM and hardness measurements. Based on the results presented and discussed, the following conclusions may be drawn:

- Starting from a super saturated solid solution and two different conditions with β'' precipitates, the samples were heat treated at 200°C. After long overaging times the hardness become similar for all starting conditions.

- Both conditions with β'' precipitates have a double peak in the hardness curve.

- The phase transition from β'' to post-β'' when overaged at 200 °C shows nucleation of post- β'' phases on β'' particles and growth of these phases.

- A simple model was proposed , and it suggested that the growth of post- β'' phases was the first steps in the transformation of β'', and that the final result was a microstructure consisting only of post- β'' particles.

- The phases observed were β'', β', U1, U2 and B'.

- The fraction of β'' starts to decrease after 180 minutes of overaging at 200°C.

- A change of the matrix/precipite interface occurs during overaging.

- A large drop in number density and volume fraction coincided with the emergence of growths on the β'' particles and the change of the matrix/precipitate interface.

Chapter 7

Further work

This work is incomplete, referring to the fact that heat treatments and hardness measurements on HT2 and HT3 were made without further investigation. Investigations of the other heat treatments should be done for comparison.

Since the transformation of β'' occurred later than expected, more HRTEM studies of the samples from HT1 with long overaging times should be investigated further to get a better understanding of the transformation. More statistical data should be collected to verify the results and the transformation mechanism proposed in the discussion.

Finally, since the Si/Mg ratio have been proven [11] to be important for which post- β'' phases that nucleate, further studies could include alloys with other Si/Mg ratios, and compare to see if a similar transformation is observed.

Bibliography

[1] Greenwood, Norman N.; Earnshaw, Alan (1997). Chemistry of the Elements (2nd ed.). Oxford: Butterworth-Heinemann. ISBN 0080379419., p. 217

[2] A. Wilm. Physikalisch-metallurgische Untersuchungen uber magnesiumhaltige Alumini- umlegierungen. Metallurgie, 8:650, 1911

[3] C.S.T.Chang, I. Wieler, N. Wanderka, and J. Banhart. Positive effect of natural pre-aging on precipitation hardening in Al-0.44 at-percent Mg-0.38 at-precent Si alloy. Ultramicroscopy, 109:585-592, 2009.

[4] ”Benefits of Recycling”. Ohio Department of Natural Resources. (2011)

[5] Donald R. Askeland and Pradeep P. Phul´e. The Scence and Enginering of Materials. Thompson, 5th edition, 2006.

[6] http://en.wikipedia.org/wiki/Burgers_vector

[7] P. Hirsch et al. Electron Microscopy of thin crystals. Robert E. Krieger, 1977.

[8] F.A. Martinsen, Clustering during Natural Aging and its Effect on Precipitation Hardening in Al-Mg-Si Alloys, Master thesis, 2011

[9] http://www.astm.org/SNEWS/MJ_2010/e0405_mj10.html

[10] D.A Porter, K.E Easterling and M.Y.Sherif, *Phase Transformations in Metals and Alloys*. Third Edition, 2008.

[11] C. D. Marioara, H. Nordmark, S. J. Andersen, and R. Holmestad. *Post-β'' phases and their influence on microstructure and hardness in 6xxx Al-Mg-Si alloys. Journal of materials science, 41:471-478, 2006.*

[12] J.D. Verhoeven. , *Verhoeven. Fundamentals of physical Metallurgy. Wiley, 1975.*

[13] J.E Hatch, *Aluminium: properties and physical metallurgy, American society for metals, Metals Park, Ohio 1984.*

[14] J. Verhoeven, *Fundamentals of Physical Metallurgy, New York: John Wiley & Sons(1975)*

[15] S. Andersen, C. marioara, A. Frøseth, R. Vissers, *Mater.Sci and Eng. A 390, 127(2005)*

[16] C. D. Marioara, S. J. Andersen, J. Jansen, and H. W. Zandbergen. Atomic model for GP zones in a 6082 Al-Mg-Si system. Acta Materialia, 49/2:321-328, 2001.

[17] S.J. Andersen, H.W. Zandbergen, J. Jansen, C. Træholt, U. Tundal, and O. Reiso, *The crystal structure of the phase in Al-Mg-Si alloys. Acta Materialia, The crystal structure of the β'' phase in Al-Mg-Si alloys. Acta Materialia, 46:3283-3298, 1998.*

[18] Håkon S. Hasting, Anders G. Frøseth, Sigmund J. Andersen, John C. Walmsley Rene Vissers and, Calin D. Marioara, Frèedèric Danoix, Williams Lefebvre, , and Randi Holmestad. *Composition of β'' precipitates in Al-Mg-Si alloys by atom probe tomography and first principles calculations. Journal of Applied Physics, 106, 2009.*

[19] S. Andersen, C. marioara, A. Frøseth, R. Vissers and H.W. Zandbergen *Mater.Sci and Eng. A 444, 157(2007)*

[20] S.J. Andersen, C.D. Marioara, R. Vissers, M. Torsæter, R. Bjørge, F.J.H. Ehlers, and R. Holmestad: Mater. Sci. Forum, 2010, vol. 638-642, pp. 390-395

[21] C.B. Carter D.B. Williams. Transmission Electron Microscopy. Springer, 1996.

[22] David Brandon and Wayne D. Kaplan. Microstructural Characterization of Materials. Wiley, 2th edition, 1984.

[23] http://en.wikipedia.org/wiki/Bragg

[24] David Brandon and Wayne D. Kaplan. Microstructural Characterization of Materials. Wiley, 2th edition, 1984.

[25] R. Vissers, J. Jansen M.A. van Huis, H.W. Zandbergen, C.D. Marioara, and S.J. Andersen, *The crystal structure of the β' phase in Al-Mg-Si alloys. Acta Materialia, 55:3815-3823, 2007.*

[26] C.D. Marioara, S. J. Andersen, H.W. Zandbergen, R. Holmestad: Met. Mater. Trans. A 36A (2005) 691–702, ISSN: 1073-5623.

[27] J. Granholt, Study of Microstructure Evolution and Change of Precipitate Structure during Overaging in an Al-Mg-Si alloy. Tapir forlag, 2011.

[28] S.J. Andersen, C D. Marioara, A. Frøseth, R. Vissers, and H.W. Zandbergen. *Crystal structure of the orthorhombic U2-Al4Mg4Si4 precipitate in the Al-Mg-Si alloy system and its relation to the β' and β'' phases. Materials Science and Engineering A, 390:127-138, 2005.*

[29] M.A. van Huis a, J.H. Chen , H.W. Zandbergen , M.H.F. Sluiter , Phase stability and structural relations of nanometer-sized, matrix-embedded precipitate phases in Al-Mg-Si alloys in the late stages of evolution, Acta Materialia 54 (2006) 2945-2955

Appendix A

TEM images

Two images from each condition from heat treament 1 (HT1) (Overaging time 0, 20, 180, 600 and 2880 min) are included as more examples from the TEM statistics, ten in total. All statistics images were taken by the author, except image 1,6 and 7. All HRTEM images are included below, and were taken by Calin D. Marioara. There are 27 images from the condition with HT1 and 600 minutes overaging, and 13 images from the condition with HT1 and 2880 minutes overaging.
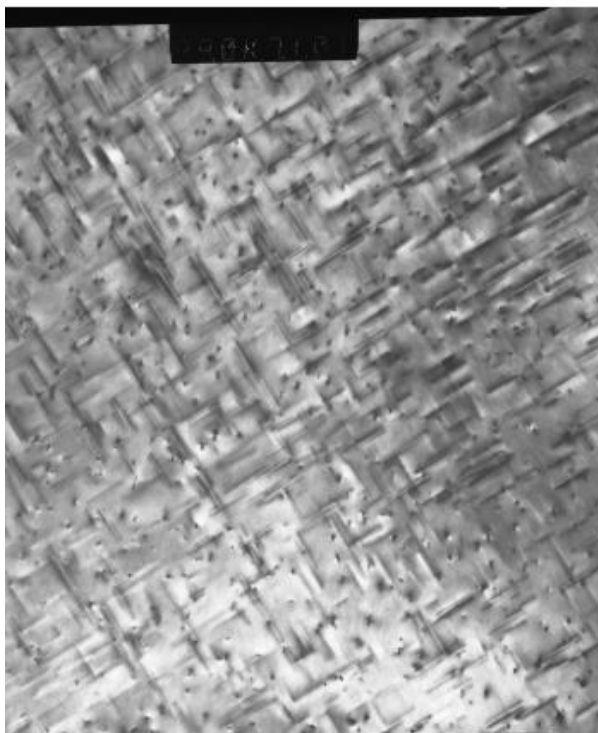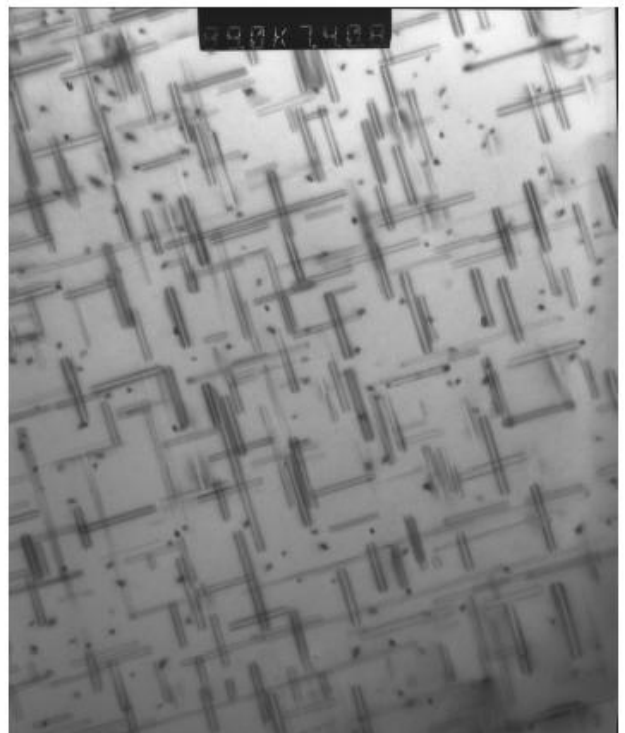
A.1 TEM statistics
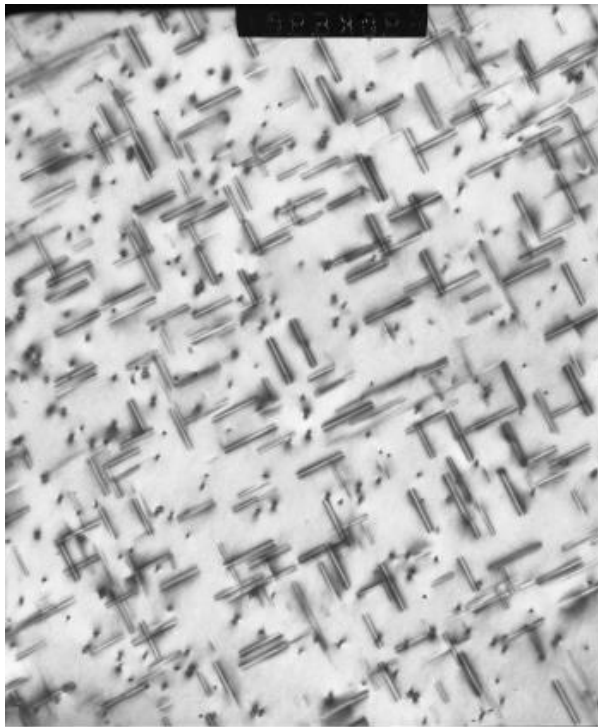
0 min OA, mag. 89 kx
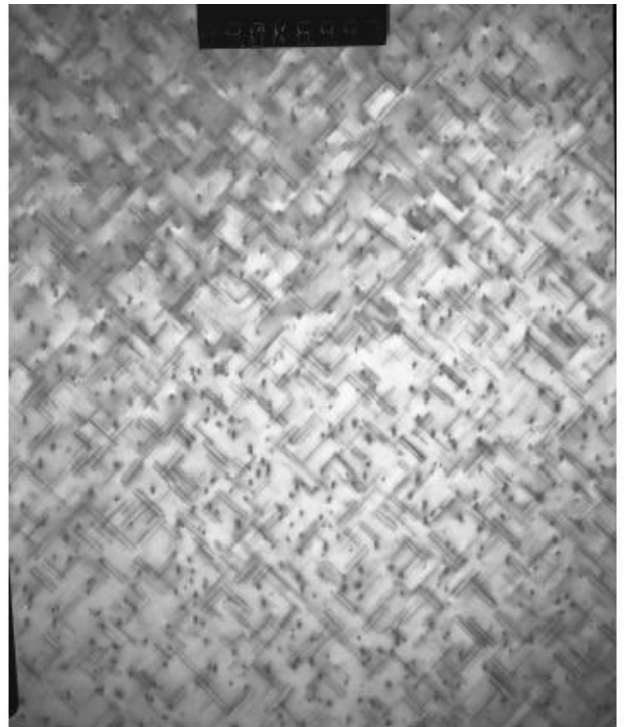
20 min OA, mag 89 kx

180 min OA, mag. 89 kx

600 min OA ,mag. 89 kx

Figure A.1: Image 1-4.
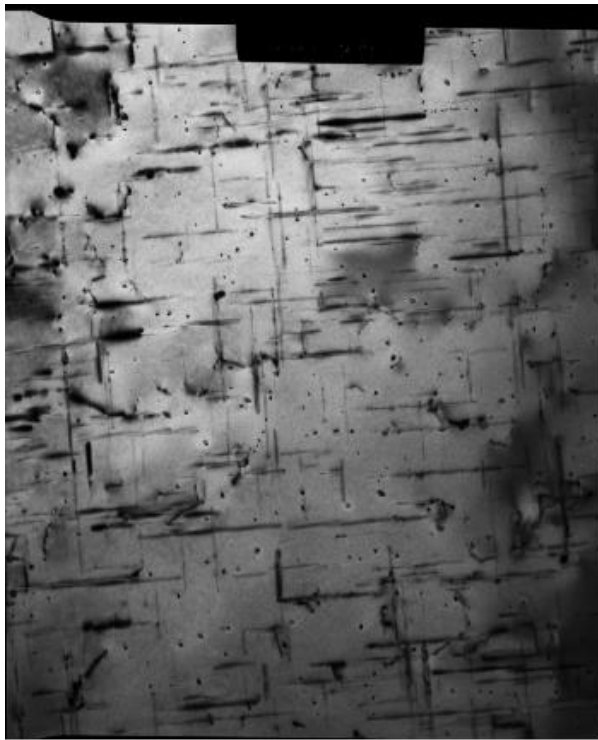
2880 min OA, mag. 31 kx
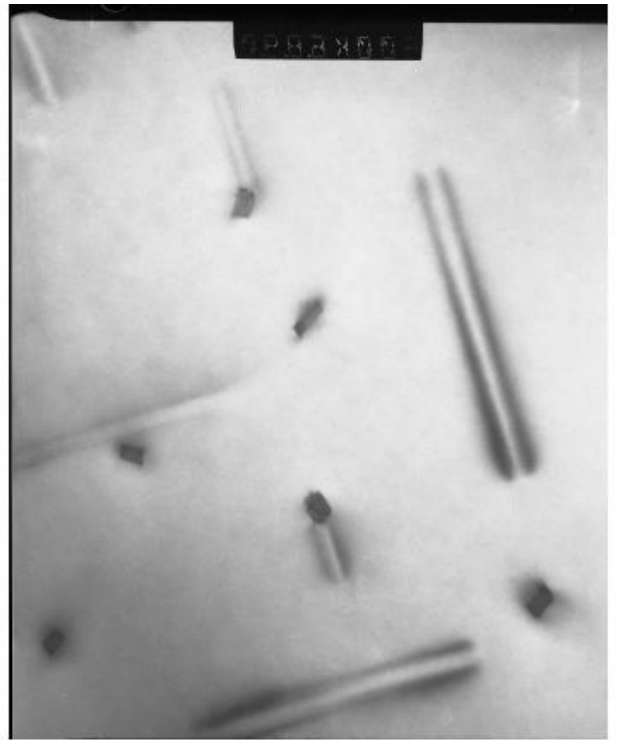
0 min OA, mag. 492 kx
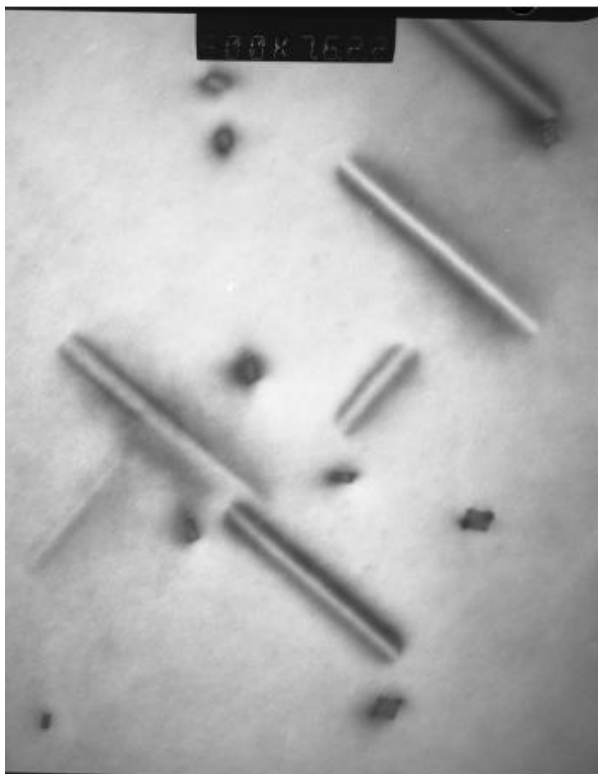
20 min OA, mag. 492 kx
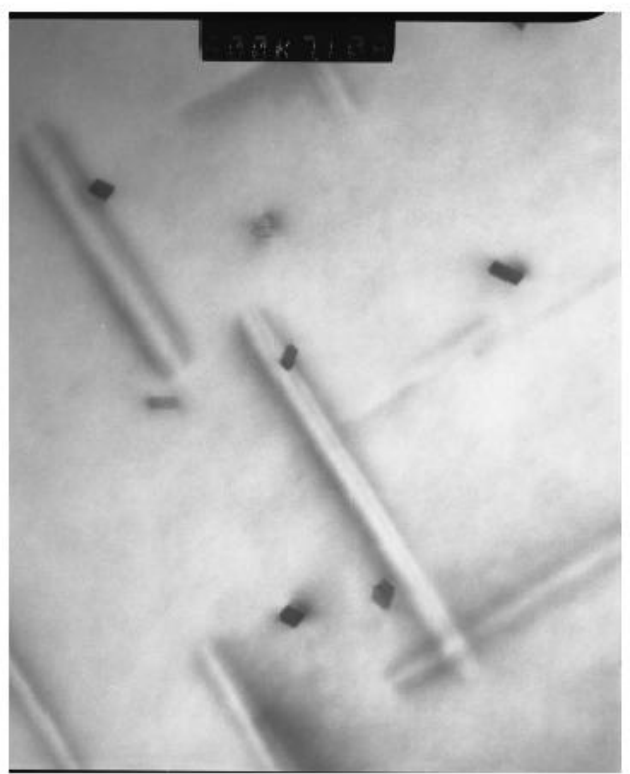
180 min OA, mag. 492 kx

Figure A.2: Image 5-8.

600 min OA, mag. 492 kx   2880 min OA, mag. 492 kx

Figure A.3: Image 9-10.

A.2   HRTEM

A.2.1   600 minutes overaging
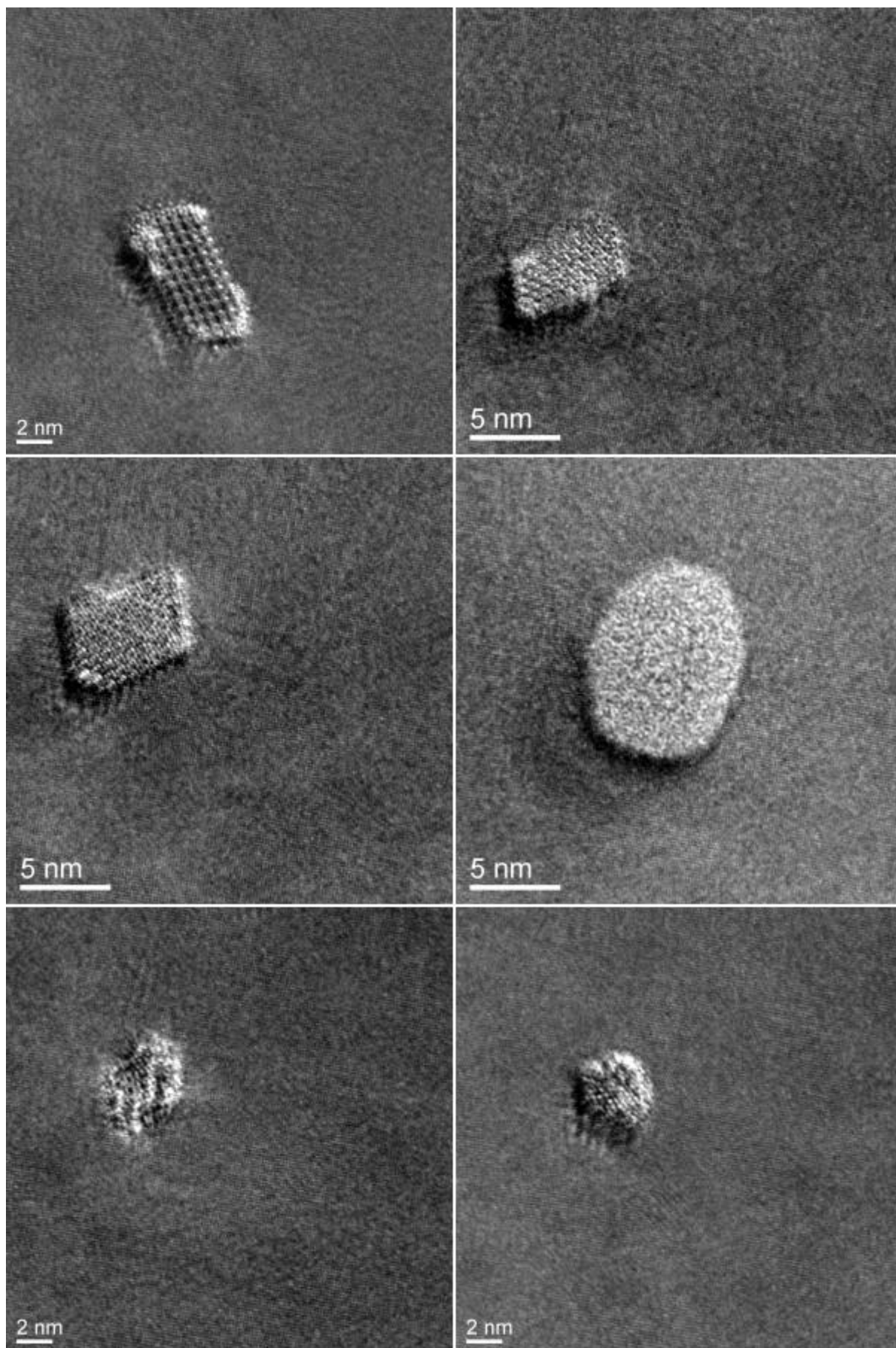
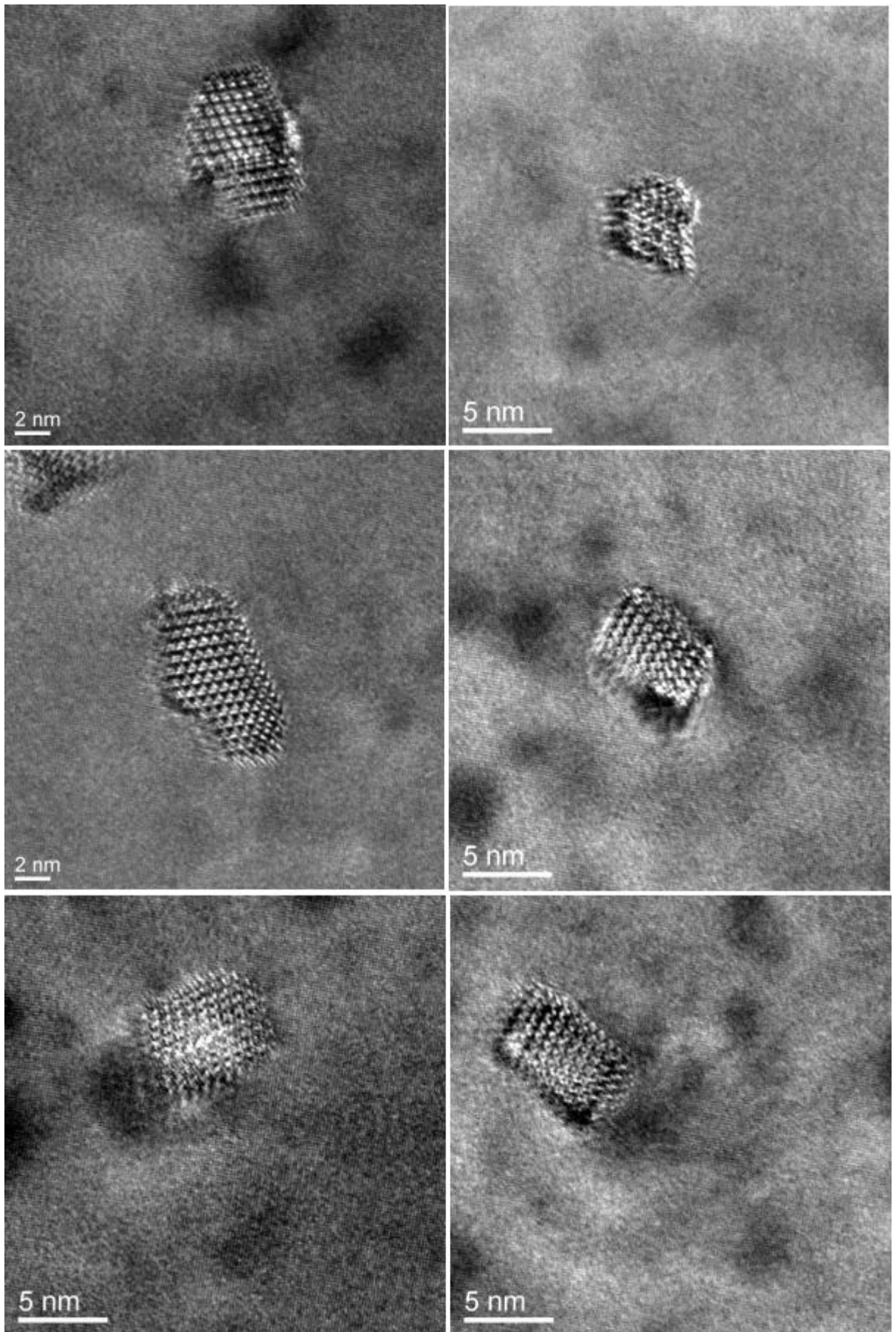Figure A.4: Image 1-6.
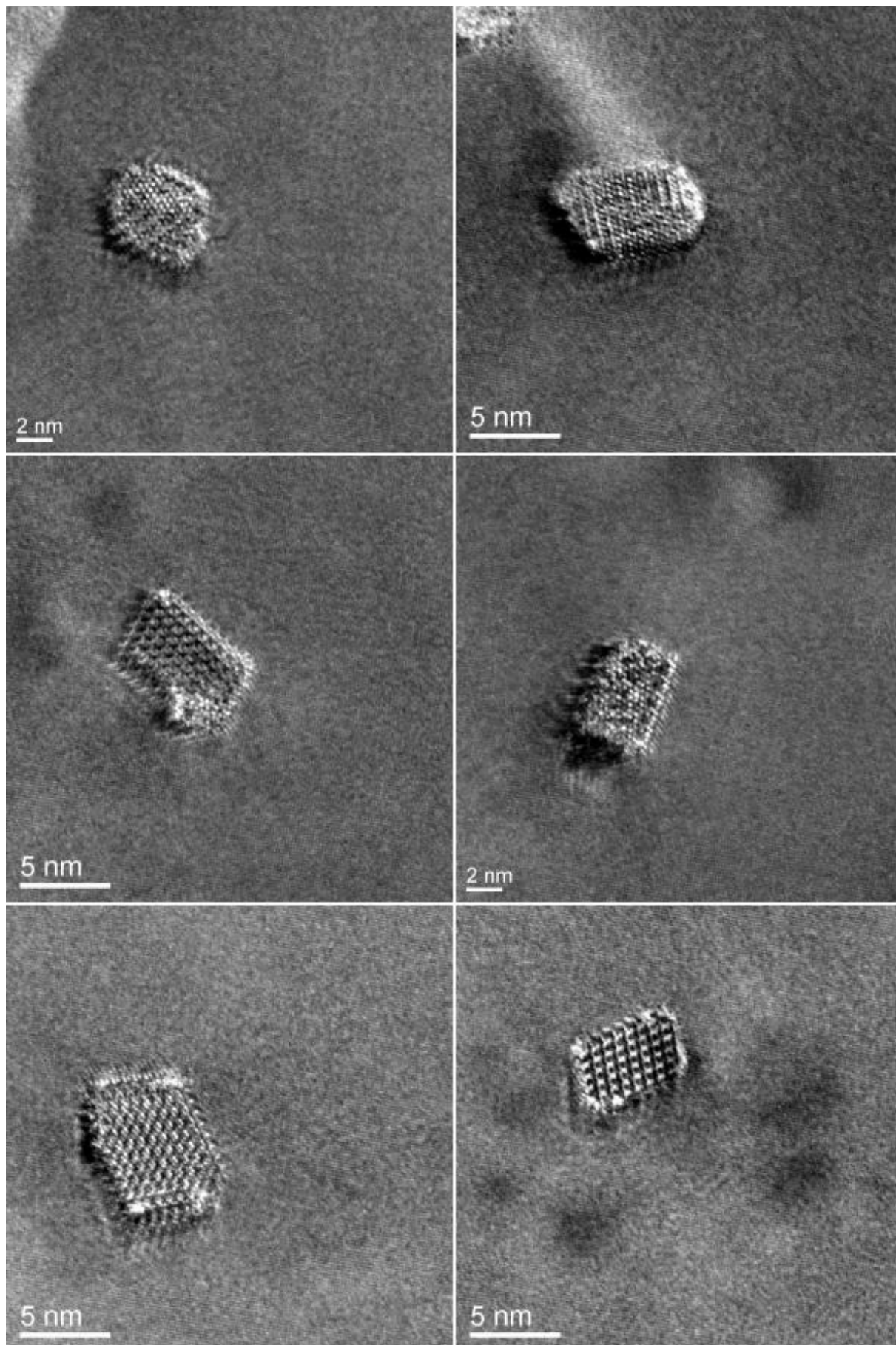
Figure A.5: Image 7-12.
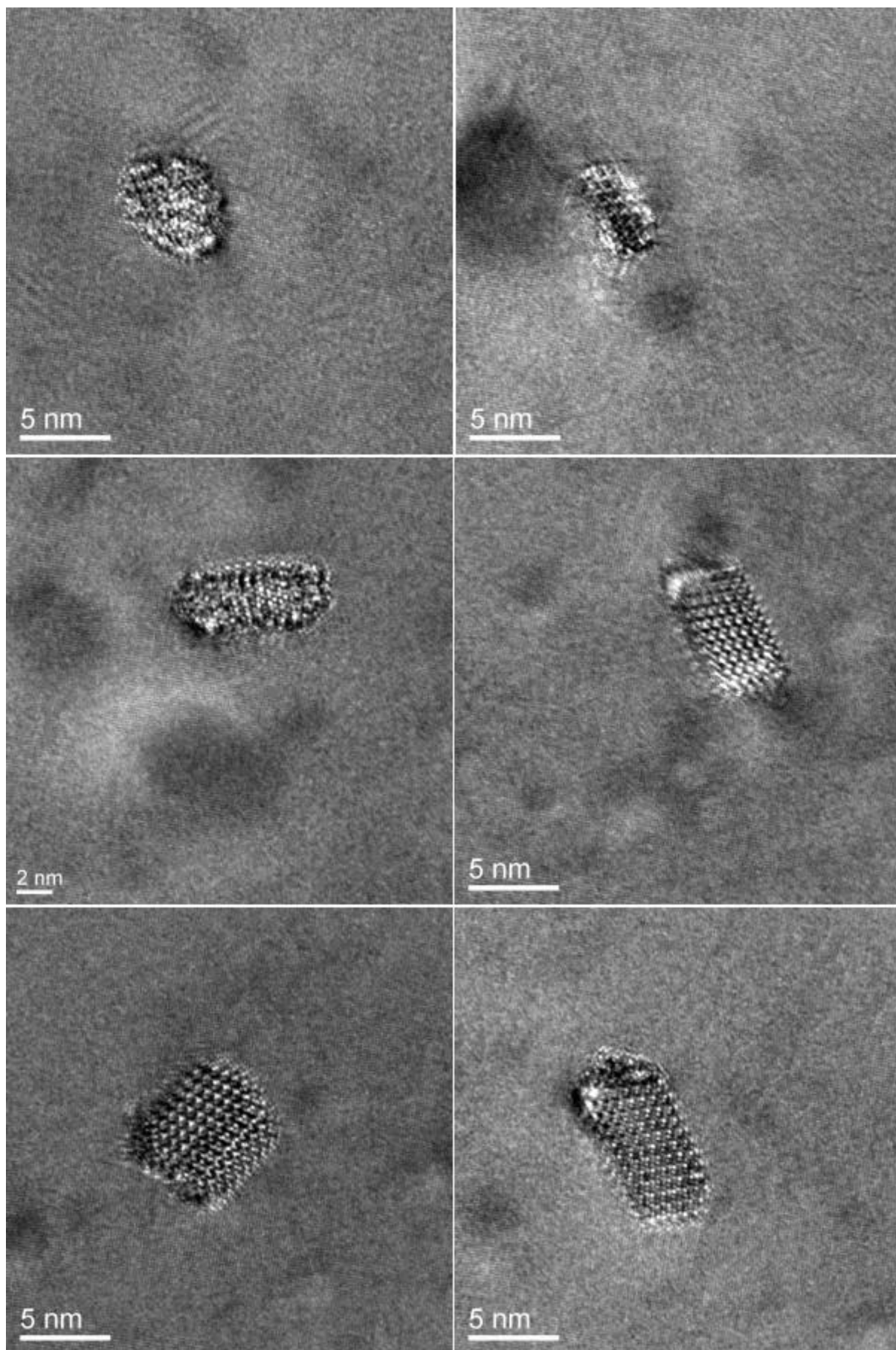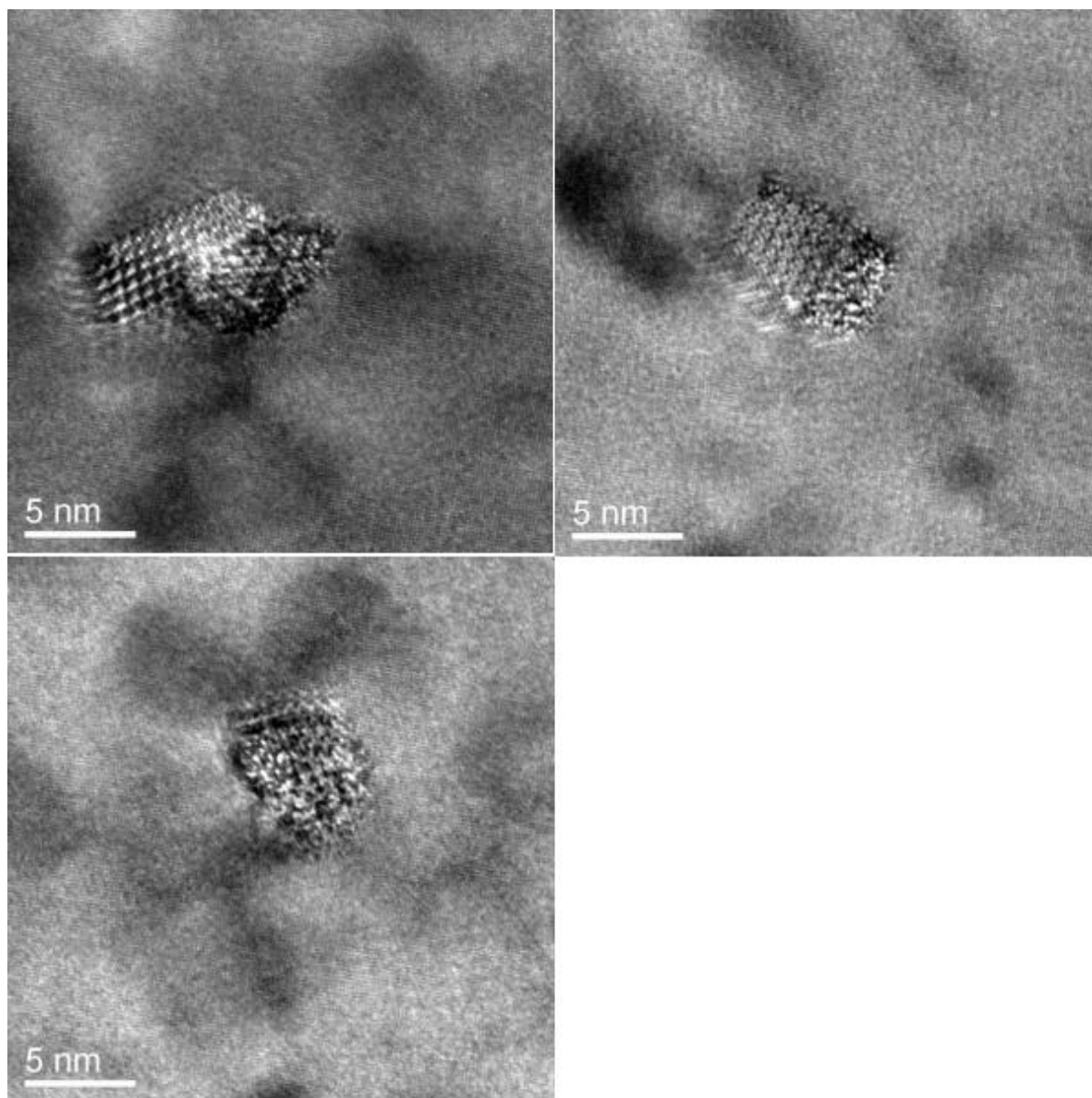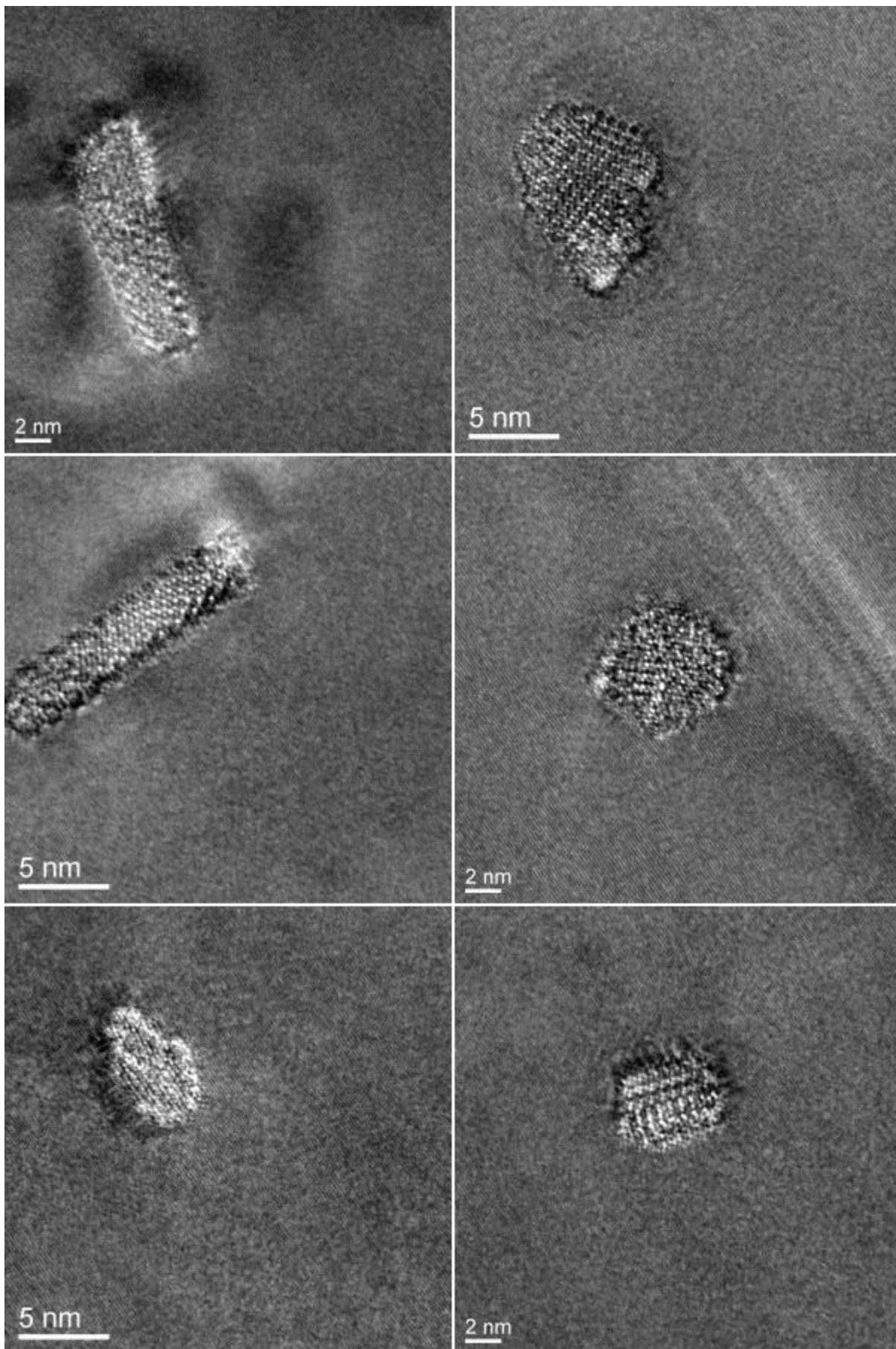
Figure A.6: Image 13-18.

Figure A.7: Image 19-24.
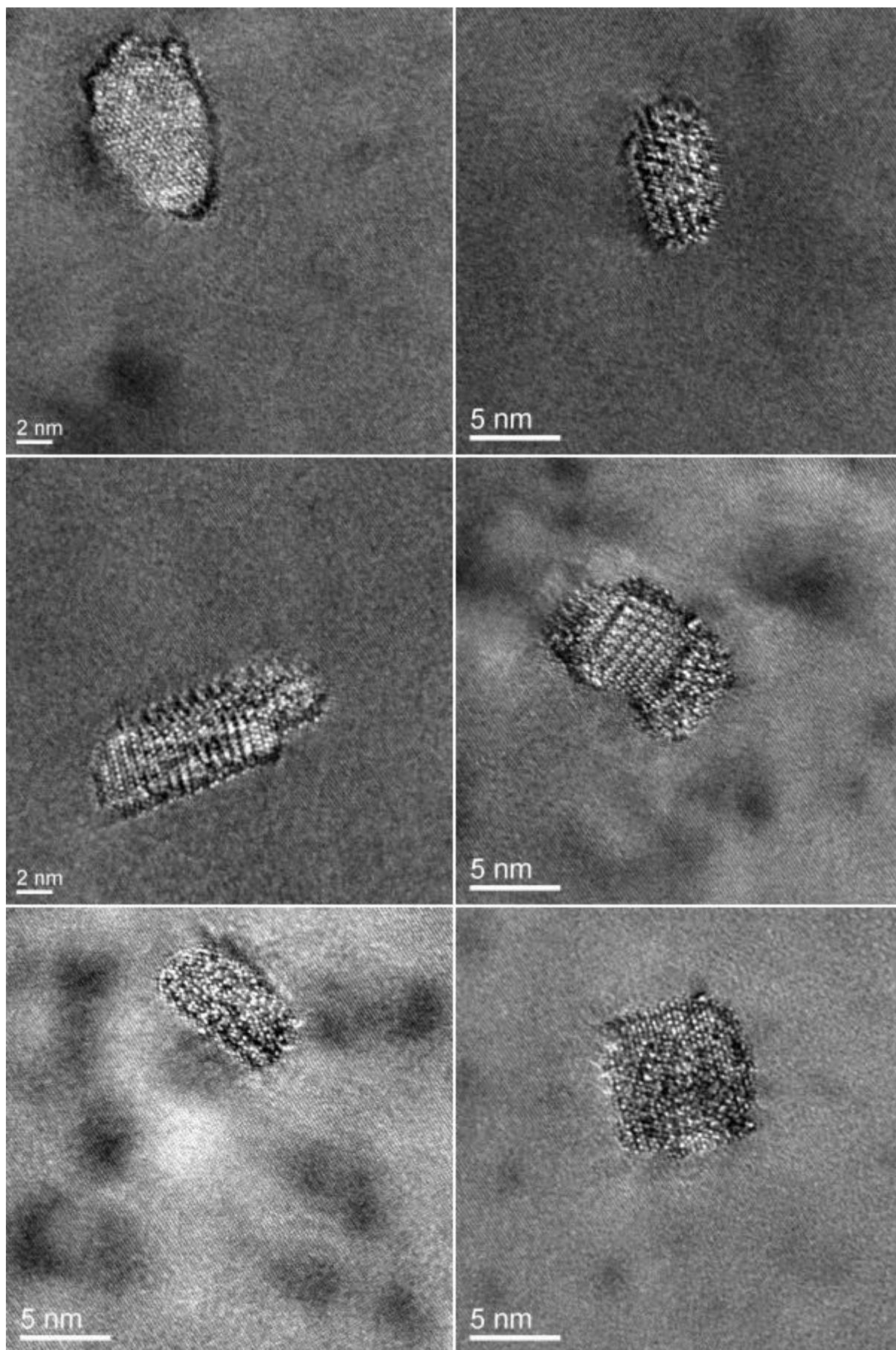
Figure A.8: Image 25-27.

A.2.2   2880 minutes overaging

Figure A.9: Image 1-6.

Figure A.10: Image 7-12.

Figure A.11: Image 13.